# Analytical Geometry Sensitivity of Droplet Spreading and Radial Recovery on Nanowall-Textured Surfaces

Najib Aminu Ismail[1] and Mubarak Yakubu[2]

[1]Department of Mechanical Engineering, Ahmadu Bello University, Zaria, Kaduna, Nigeria
[2]Khalifa University, Abu Dhabi 127788, United Arab Emirates

**Abstract**

Whether an impacting drop stays where it lands or recoils matters for anti-icing, self-cleaning, spray deposition and cooling on water-repellent textured surfaces. Reduced-order models of impact on nanowall textures have so far been integrated numerically, so the conditions that separate these outcomes have not been expressed in closed form. We solve analytically the first impact cycle of a nonlinear radial oscillator with saturated contact-line pinning. Two explicit critical pinning forces, $P_c$ and $P_s$, divide the outcomes into sticking at maximum spread, recoil arrest at a residual radial extent given by a cubic, and radial return. Their ratio $P_s/P_c$ depends only on the product of stiffness and impact energy and lies between $2\sqrt{2/3} \approx 1.63$ and $4(2/5)^{3/4} \approx 2.01$. The corresponding ratio of boundary spacings, $(P_s/P_c)^{1/(1-\nu)}$, is 1.93 for a spacing-independent edge force ($\nu = 0$) but 3.72 for $\nu = 0.5$, so geometric criteria depend on the assumed force-scaling law. Written as contact-angle hysteresis, $P = \frac{3}{2}(\cos\theta_r - \cos\theta_a)$, the force thresholds become wetting thresholds, and hysteresis alone cannot hold a drop at maximum spread above $\mathrm{We} \approx 11$. The measured hysteresis of the nanowall surfaces of Yilbas et al. (about $4^\circ$ at $158^\circ$) gives $P \approx 0.04$ and places those impacts in radial return, whereas the inherited geometric closure gives $P \approx 4.4$, more than any hysteresis can supply. The spacing boundaries derived from that closure (about 67 and 129 nm at $\mathrm{We} = 18.3$ for $\nu = 0$) are therefore scenario predictions, not validated thresholds. Closed-form inverse relations recover the stiffness and pinning force from two observables of one impact; with 3% measurement noise the pinning force is recovered to within about 10–20%, but the stiffness only to within $-34\%$ to $+56\%$. The results describe a single radial coordinate with saturated pinning and a prescribed Cassie state. They do not predict detachment, retained liquid volume or normal restitution, and they are offered as design hypotheses to be tested by spacing-series impact experiments.

**Keywords:** droplet impact; nanowall texture; contact-line pinning; contact-angle hysteresis; recoil regimes; residual radial extent; analytical model; global sensitivity analysis

## 1 Introduction

When a drop strikes a water-repellent surface, its kinetic energy is converted within a few milliseconds into surface energy, internal flow and heat. How far the drop spreads sets the largest area it wets, while what happens next (recoil, partial retraction or rebound) depends on how much of the stored energy is returned. Both matter in coating, cleaning, anti-icing and cooling. Simple analytical models are valuable here because they show which force mechanism controls each measurable response, and they make it possible to separate those mechanisms from the assumptions made about surface geometry.

The roles of inertia, capillarity and viscous dissipation in spreading are well established [1]. Clanet et al. [2] identified an inertia–capillary scaling for the maximum deformation. Oscillator models give a complementary view of how capillary energy is stored and released: Okumura et al. [3] treated a bouncing drop as a water spring, and Kim and Chun [4] used a spring–mass–damper analogue to describe recoil after impact. The present approach follows this line of reduced-order energy models, with the caveat that a single deformation coordinate cannot capture the internal flow or the motion of the center of mass.

Texture adds geometric and wetting constraints. A drop may rest on top of the texture in the Cassie–Baxter state [5] or fill it in the Wenzel state [6], and an impact can push liquid from one state into the other. Bartolo et al. [7] measured this impalement transition on micropatterned superhydrophobic surfaces. Tsai et al. [8] found that micro- and nanostructured surfaces with similar static contact angles respond differently to impact, so static wettability alone does not determine the dynamics. Spacing matters as well: on hydrophobic PDMS micro-post arrays, wider post spacing limits how far an impacting drop spreads, and the impact itself can remove dust from the surface [9]. Any geometry-dependent resistance law therefore has to be read together with the wetting state it assumes.

Texture can also redirect momentum during recovery. Bird et al. [10] shortened the contact time by breaking the symmetry of recoil, and Liu et al. [11] observed pancake bouncing, in which drops leave the surface while still flat, before radial retraction is complete. These observations show that radial return and lift-off are different events, and that a model of the radial motion should not be read as a model of rebound.

This study concerns nanowall-textured silicon. Yilbas et al. [12] found that such surfaces reduce the maximum spread, and they discussed how liquid penetration and trapped gas affect rebound. In our previous work [13] we developed a nonlinear radial model in which deformation is governed by capillary stiffness, viscous damping, kinetic resistance and a static-arrest condition. Its pore closure scales the edge force in proportion to the spacing, so the effective resistance does not depend on spacing at all. A natural question follows: how do spreading and recovery change when the edge-force scale and the spacing follow different geometric laws? Answering it requires separating the effects of encounter density, edge resistance, nonlinear stiffness and damping before any spacing trend is turned into a design recommendation.

The present paper builds directly on [13], and it is useful to state what is inherited and what is new. That work formulated the equation of motion (2), the time and energy scales, the damping closure and the proportional-pore pinning closure, calibrated $\kappa = 6$, $\zeta_0 = 0.70$ and the reference edge scale at a single impact condition, and integrated the model numerically with a finite smoothing speed. Everything else here is new: the saturated-pinning solution of the first cycle (amplitude equation, quadratures, the closed-form thresholds $P_c$ and $P_s$, the residual-extent cubic and the bounds on $P_s/P_c$), the phase-plane construction, the inverse relations and their noise analysis, the family of edge-scaling exponents, the global sensitivity analysis, the hysteresis form with its admissibility bound and the comparison with measured wetting data, the energy partition, the event times and the energy-projection analysis. Because [13] used proportional scaling ($\nu = 1$ below), its spacing-independent results are one member of the present family.

Three questions remain open. First, there is no closed-form criterion that tells, for a given texture spacing and impact speed, whether a drop will stick, stop part-way through recoil or return. Reduced-order models, including our own, have so far been integrated numerically, so the regime boundaries appear only as features of parameter maps and their dependence on the model parameters is hidden. Second, the pinning force in these models comes from a geometric closure whose force scale is poorly constrained, and it is not known which predictions survive that uncertainty. Third, the model force has not been connected to a property that can be measured on a real surface,

such as contact-angle hysteresis, which leaves the closure without a physical check.

We address these questions analytically. In the limit of saturated resistance the first impact cycle of the model can be solved analytically, which gives a unique maximum-spread equation, trajectory quadratures, explicit regime boundaries and exact sensitivities to geometry. A first-order viscous correction measures the effect of the width-to-pitch ratio, a variance-based global sensitivity analysis ranks the uncertain closure inputs, and an equivalent hysteresis form of the pinning force links the model to measurable wetting properties, which we use to compare the closure with the measured wetting of the nanowall surfaces of [12]. Throughout, we compare fixed, intermediate and proportional edge scaling at a common reference geometry.

The main results are the following. (i) We derive a closed-form stick boundary to accompany the return boundary. Together they sort every first-cycle outcome into three regimes, and a cubic equation gives the residual extent left by arrested recoil. When the pinning force decreases with spacing, this residual radial extent is non-monotonic in spacing. (ii) The ratio of the two critical forces, $P_s/P_c$, depends on $\kappa H$ alone and lies within proven bounds. The corresponding ratio of boundary spacings, $a_c/a_s = (P_s/P_c)^{1/(1-\nu)}$, does not depend on the edge-force magnitude, but it depends strongly on the edge-scaling exponent $\nu$, and observing it would determine that exponent. (iii) Explicit inverse relations recover the stiffness and the pinning force from the maximum spread combined with either the recovery speed or the residual extent, and we quantify their robustness to 1–5% measurement noise, near the regime boundaries and across impact speeds. (iv) A variance-based global sensitivity analysis ranks the uncertain inputs across the spacing range and shows which measurement would reduce the predictive uncertainty most at each spacing. (v) Comparison with established maximum-spread correlations bounds the inherited stiffness calibration for $2 \leq \mathrm{We} \leq 200$. (vi) Expressing the pinning force as an equivalent contact-angle hysteresis turns the force thresholds into measurable wetting thresholds and gives a physical admissibility test for the geometric closure. Applied to the measured hysteresis of the surfaces of [12], it shows that the inherited closure force is about a hundred times larger than hysteresis can supply. (vii) An exact energy partition separates outward and inward pinning work, stored deformation energy and recovered kinetic energy in all three regimes. (viii) Closed-form event times show how pinning changes the spreading and recoil durations and reveal a maximum of the recoil time at the return boundary. (ix) Varying the fraction of impact energy assigned to radial motion, and the stiffness, shows which predictions are robust to the two main modelling assumptions of the oscillator. Section 6.4 gathers these results into quantitative predictions that experiments can falsify, and Section 6.6 states the limitations of the approach and the work needed to remove them. The paper is organized as follows. Section 2 presents the model, the geometry closures and the baseline parameters, illustrated in Fig. 1. Section 3 derives the exact solution, the three regimes (Fig. 2) and their phase-plane geometry (Fig. 3), together with the inverse relations and the hysteresis form. Section 4 adds the weak-viscosity correction and its verification. Section 5 reports the parametric results, Section 6 discusses their implications, limitations and future work, and Section 7 concludes.

# 2 Model, geometry, and parameter status

## 2.1 Effective radial dynamics

Let $r(t)$ denote an effective radial extent with reference value $r_0 = D_0/2$; it should not be confused with the wetted contact radius at first contact. As in [13], we take $r(0) = r_0$ and $\dot{r}(0) = U_0$, and the lumped mass equals the mass of the drop. Assigning the impact speed to the radial coordinate is a projection assumption: it places the incident kinetic energy in this coordinate without resolving the velocity field inside the drop. Section 5.11 quantifies its consequences by assigning only a fraction

$\eta$ of that energy to the radial motion.

The coordinate $r$ is therefore an effective radial deformation of the drop. It is distinct from four quantities that experiments record: the projected (apparent) diameter seen from the side or from above, the wetted contact radius, the residual wetted area once motion stops, and the volume of liquid that stays on the surface. We compare $\beta = r/r_0$ with the measured spread factor only at maximum spread, where the lamella is thin and the projected and wetted diameters are close (Section 5.6); no mapping between $r$ and the wetted radius is assumed during recoil. In what follows, *sticking* means that the effective radial extent stops at its maximum, *recoil arrest* that it stops between the maximum and the reference value, and *radial return* that it reaches the reference value with nonzero inward speed. *Normal rebound*, *detachment*, *wetted footprint* and *deposited area* denote physical events and quantities that the model does not resolve, and we do not treat them as interchangeable with these model outcomes. In particular, radial return means only that $r$ has come back to $r_0$; it does not imply that the contact radius has vanished, that the drop has detached, or that no liquid remains.

Set $x = (r - r_0)/r_0$, $s = t/\tau$, and

$$m = \rho V, \quad k = \frac{4\pi\gamma}{3}, \quad \tau = \sqrt{\frac{m}{k}} = \sqrt{\frac{\rho D_0^3}{8\gamma}}, \quad Q = \frac{U_0\tau}{r_0} = \sqrt{\frac{\mathrm{We}}{2}}. \tag{1}$$

The equation of motion, taken from [13], is

$$x'' + x + \kappa x^3 + 2\zeta x' + P\tanh(x'/\epsilon) = 0, \quad x(0) = 0, \quad x'(0) = Q, \tag{2}$$

with $P = F_{\mathrm{pin}}/(kr_0)$ and $\epsilon = v_s\tau/r_0$. Define

$$\mathcal{U}(x) = \tfrac{1}{2}x^2 + \tfrac{\kappa}{4}x^4, \qquad H = \tfrac{1}{2}Q^2. \tag{3}$$

Energies are scaled by $kr_0^2$. In the analytical model we let $\epsilon \to 0$, so that the kinetic resistance becomes $P\,\mathrm{sgn}(x')$ while the contact line moves. When the drop is at rest, a static reaction balances the restoring force as long as that force does not exceed $P$; equal static and kinetic capacities correspond to the unit static-capacity factor of [13]. A turning point at positive $x$ therefore sticks if $\mathcal{U}'(x) \le P$. The motion ends at the first sticking event or at the first retracting crossing of $x = 0$, and we do not continue it to negative radius.

Figure 1 shows how the surface geometry enters the oscillator. Each element of the analogue carries one energy pathway. The nonlinear spring stores surface energy as the drop flattens, and its quartic term stiffens the response at large deformation; this term produces the inertia–capillary scaling discussed in Section 6.1. The dashpot dissipates energy at a rate set mainly by the Reynolds number and only weakly by the solid fraction. The dry-friction contact stands for contact-line pinning at the wall edges. Because it can transmit any force up to $P$ without sliding, the system has a whole interval of rest states instead of a single equilibrium, as in any Coulomb oscillator, and this is what allows a drop to stay spread after impact. The pitch sets how many wall edges the contact line crosses and hence the size of $P$, whereas the width-to-pitch ratio affects only the damping. This division explains why the spacing and ratio effects in Section 5 differ by more than an order of magnitude.

## 2.2 Geometry closures

The study uses

$$40 \le a \le 400\ \mathrm{nm}, \quad 0.05 \le \alpha = \frac{w}{2a} \le 0.60, \quad \phi = \alpha^2. \tag{4}$$

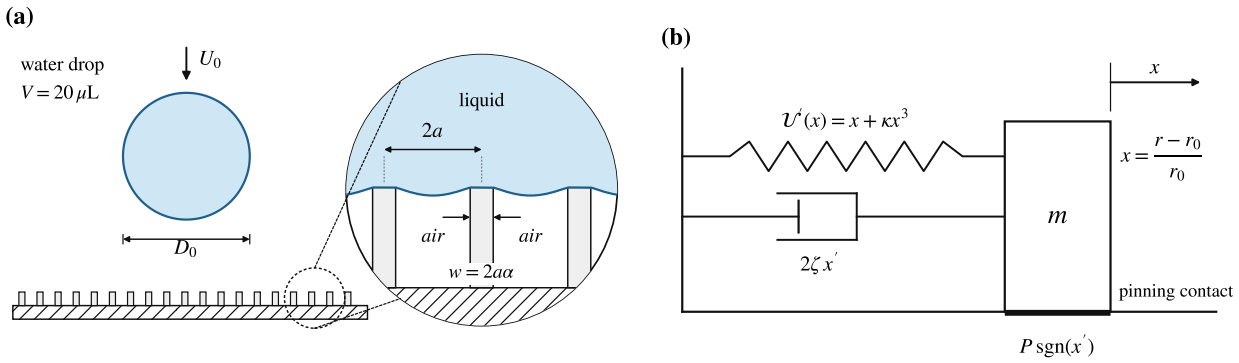


Figure 1: Physical setting and its reduced-order representation. (a) A water drop of volume $V = 20\ \mu$L and diameter $D_0$ impacts the nanowall texture at speed $U_0$. The magnified inset shows the assumed Cassie (suspended) state, in which the liquid rests on the wall tops with menisci spanning the air gaps. The pitch is $2a$, the wall width is $w = 2a\alpha$, and the square-element planform fraction is $\phi = \alpha^2$. Wall height does not enter the model. (b) Lumped analogue of equation (2) in the scaled variables, where the mass is unity because forces are scaled by $kr_0$ and time by $\tau$. The spring carries the capillary restoring force $\mathcal{U}'(x) = x + \kappa x^3$, the dashpot carries the viscous force $2\zeta x'$, and the dry-friction contact carries the saturated pinning force $P\,\mathrm{sgn}(x')$. The texture enters only through $P(a)$, equation (5), and $\zeta(\alpha)$, equation (7). The schematic is not to scale.

Here $2a$ is the pitch and $w = 2a\alpha$ the wall width. The relation $\phi = \alpha^2$ treats the texture as square elements; it is a modeling idealization rather than a measured area fraction, and a continuous wall network would need a different expression. Note also that $\alpha$ is a width-to-pitch ratio, not an aspect ratio, since wall height does not appear in the model.

With fixed-reference encounter count $n_0 = \pi r_0/a$,

$$P = \frac{3\pi}{4}\frac{D_e(a)}{a}|\cos\theta^*|, \quad D_e(a) = D_{e,r}\left(\frac{a}{a_r}\right)^{\nu}. \tag{5}$$

The effective edge length $D_e$ is a phenomenological force scale, not a resolved hydraulic diameter. With $a_r = 65$ nm and $D_{e,r} = 130$ nm, the case $\nu = 1$ reproduces the proportional-pore closure $D_e = 2a$ of [13]. The reference value $a_r = 65$ nm comes from the average spacing of about 130 nm reported for the surfaces of [12]. That paper describes $2a$ as the spacing between two consecutive walls and writes the solid fraction as $\phi \approx w^2/4a^2 \approx 0.3$. If its spacing is a centre-to-centre pitch, it maps directly onto our $2a$. If it is the clear gap between walls, the corresponding half-pitch is $a_r/(1-\alpha)$, about 1.4 times larger for $\alpha = 0.3$, and its solid fraction refers to a different normalization. The published description does not settle this, so $a_r$ carries at least this uncertainty. We take $\nu = 0$ (fixed edge) as the main scenario and use $\nu = 1/2$ and 1 to test the structural uncertainty. Therefore

$$\frac{\partial \ln P}{\partial \ln a} = \nu - 1. \tag{6}$$

The cancellation at $\nu = 1$ is a property of the chosen geometry, not a numerical artifact or a general physical insensitivity. Likewise, holding $D_e$ fixed defines a different family of model surfaces; it does not show that real nanowalls belong to that family.

The exponent $\nu$ describes how the pinning force per wall encounter changes with pitch. The fixed-edge case $\nu = 0$ corresponds to a force per encounter set by a length that does not scale with the pitch, such as a fixed wall-top width, edge defects or a fixed meniscus attachment length; the

resistance then grows with the number of walls crossed, $P \propto 1/a$. The proportional case $\nu = 1$ corresponds to geometrically similar textures, for which classical wetting models make hysteresis depend on the solid fraction rather than on the absolute size, so that $P$ is independent of $a$ at fixed $\alpha$. Intermediate values describe partial scaling, for example a wall width that grows more slowly than the pitch. The encounter density $n_0 = \pi r_0/a$ assumes that the contact line crosses one wall per pitch along its perimeter. In a connected wall network, where parts of the contact line may lie along walls rather than across them, the effective count depends on topology and orientation and is better treated as part of the uncertain edge scale. Wall height enters only through the wetting state. In [12] the walls are about 10 $\mu$m tall and the measured liquid penetration during impact was about 0.04 $\mu$m, so the Cassie assumption is reasonable for those surfaces at the tested speeds, but impalement on shorter or more widely spaced walls would change the resistance law altogether. No experiment has yet discriminated among these scenarios. We therefore use $\nu = 0$ as the main illustrative case, not as the established law, report spacing criteria as scenario-dependent predictions, and give in Section 6.6 the minimum measurements that would fix $\nu$.

Viscosity enters through

$$\zeta = \frac{\zeta_0(1+\alpha^2)}{\sqrt{\mathrm{Re}}}. \tag{7}$$

The apparent contact angle is prescribed. None of these closures predicts penetration, wall compliance, gas drainage or wetting transitions, and the factor $|\cos\theta^*|$ comes from the chosen force estimate rather than from a measured advancing–receding hysteresis.

### 2.3 Baseline and provenance

Water properties are $\rho = 998\ \mathrm{kg\,m^{-3}}$, $\mu = 10^{-3}\ \mathrm{Pa\,s}$, and $\gamma = 0.072\ \mathrm{N\,m^{-1}}$. For $V = 20\ \mu$L and $h = 20$ mm,

$$D_0 = (6V/\pi)^{1/3}, \qquad U_0 = \sqrt{2gh}, \quad g = 9.81\ \mathrm{m\,s^{-2}}. \tag{8}$$

Ignoring air drag during the fall gives $D_0 \simeq 3.368$ mm, $U_0 \simeq 0.6264\ \mathrm{m\,s^{-1}}$, $\mathrm{We} \simeq 18.32$, $\mathrm{Re} \simeq 2105$ and $\mathrm{Oh} \simeq 0.00203$, and the oscillator time is $\tau \simeq 8.135$ ms. The diameter-based scale $\sqrt{\rho D_0^3/\gamma} = \sqrt{8}\tau$ is sometimes used instead, but it is not the natural time of the oscillator and should not replace $\tau$. The stiffness $\kappa$ is an aggregate correction for drop deformation, not a material property of the

Table 1: Parameter status; closures are fixed across samples.

| Quantity | Value | Status |
|---|---|---|
| $m$, $k$, $Q$, $H$ | Equations (1)–(3) | Derived under projection assumptions |
| $\kappa$ | 6.0 (4–8) | Calibrated at $\mathrm{We} = 18.3$ in [13] |
| $\zeta_0$ | 0.70 | Damping prefactor from [13] |
| $\theta^*$, $\Delta\theta$ | 158°, 4° | Measured apparent angle and hysteresis [12] |
| $\eta$ | 1 (0.5–1) | Radial energy fraction; projection assumption |
| $D_{e,r}$, $a_r$ | 130 nm, 65 nm | Assumed effective scale and reference |
| $\nu$ | 0, 0.5, 1 | Structural scenarios |
| Static/kinetic capacity | 1 | Hybrid-model assumption |

nanowalls, and the available information does not support a physical confidence interval for the edge scale. The value $\kappa = 6$ was calibrated in [13] at the baseline impact condition only, so its calibration range is effectively that single point. Section 5.6 compares it with smooth-surface correlations at other speeds, and Section 5.11 shows how values between 4 and 8 move the thresholds.

## 3 Analytical first-cycle solution

We call a result *exact* when it holds without approximation within the zero-viscosity, saturated-pinning model. Some exact results are explicit closed forms: the thresholds $(A_c, P_c)$ and $(A_s, P_s)$, the recovery $e_r$, the inverse relations and the bounds on $P_s/P_c$. Others are exact algebraic or integral representations that we evaluate numerically: the amplitude $A$ is the root of a quartic and the residual extent $B$ the root of a cubic, both found by bracketed root finding, and event times and viscous integrals are quadratures evaluated adaptively. The weak-viscosity results of Section 4 are first-order approximations, and the piecewise ODE integrations are independent numerical checks of the mathematics, not physical validation.

### 3.1 Maximum spread and implicit trajectory

For $\zeta = 0$, multiplying the outward equation by $x'$ and integrating gives $x'^2/2 = H - \mathcal{U}(x) - Px$. The maximum extension $A$ is therefore the unique positive root of

$$\mathcal{U}(A) + PA = H, \qquad \beta_{\max}^{(0)} = 1 + A. \tag{9}$$

The root is unique because $\mathcal{U}'(A) + P > 0$, and solving this monotone quartic numerically is simpler than working with its radical form. The outward trajectory is given exactly by

$$s(x) = \int_0^x \frac{du}{\sqrt{2[H - \mathcal{U}(u) - Pu]}}. \tag{10}$$

If the drop recoils, its kinetic energy and the elapsed time on the inward leg are

$$K_r(x) = \mathcal{U}(A) - \mathcal{U}(x) - P(A - x), \tag{11}$$

$$s(x) - s(A) = \int_x^A \frac{du}{\sqrt{2K_r(u)}}. \tag{12}$$

The square-root singularities at the end points are integrable. The quadratures thus give the trajectory from energy alone, without time-stepping the model. They describe radial event times, which are not the same as physical contact times.

### 3.2 Radial-return boundary and recovery

We define the radial recovery $e_r$ as $|x'|/Q$ at the first retracting crossing of $x = 0$, and set $e_r = 0$ if the drop sticks first. For return with positive speed,

$$e_r^{(0)} = \sqrt{1 - \frac{2PA}{H}}. \tag{13}$$

The outcome is decided in two steps. If $\mathcal{U}'(A) \le P$, the drop sticks at maximum spread; otherwise it recoils. Recoil reaches $x = 0$ with positive speed only if $H > 2PA$. When $H < 2PA$, equation (11) has a smaller positive zero $B$ at which recoil stops, and convexity of $\mathcal{U}$ gives $\mathcal{U}'(B) < P$, so the static reaction can hold the drop there. In the borderline case $H = 2PA$ the drop reaches $x = 0$ with zero speed.

Eliminating $P$ between the amplitude equation and the condition of zero return energy gives

$$A_c^2 = \frac{-1 + \sqrt{1 + 2\kappa H}}{\kappa}, \qquad P_c = \frac{\mathcal{U}(A_c)}{A_c}. \tag{14}$$

In the linear limit $\kappa \to 0$, $A_c = \sqrt{H}$ and $P_c = \sqrt{H}/2$. For a fixed edge, $P = C/a$ with $C = (3\pi/4) D_{e,r} |\cos\theta^*|$, so the boundary spacing is $a_c = C/P_c$. This is a boundary of the analytical model; it should not be read as a measured critical spacing or a lift-off criterion.

### 3.3 Stick boundary, three regimes, and residual extent

The sticking condition $\mathcal{U}'(A) \le P$ also leads to a closed-form boundary. Setting $P = \mathcal{U}'(A_s)$ in the amplitude equation gives $\mathcal{U}(A_s) + A_s\mathcal{U}'(A_s) = H$, that is, $\frac{3}{2}A_s^2 + \frac{5}{4}\kappa A_s^4 = H$, so that

$$A_s^2 = \frac{-3 + \sqrt{9 + 20\kappa H}}{5\kappa}, \qquad P_s = A_s + \kappa A_s^3. \tag{15}$$

Since $A$ decreases monotonically with $P$, every first-cycle outcome belongs to one of three regimes: sticking at maximum spread for $P \ge P_s$, arrested recoil for $P_c < P < P_s$, and radial return for $P < P_c$ (Fig. 2). Whenever $P$ decreases with $a$, these become spacing boundaries; under the fixed-edge closure they are $a_s = C/P_s$ and $a_c = C/P_c$. In the arrest regime the residual extent $B \in (0, A)$ follows from $K_r(B) = 0$ after dividing by $A - B$:

$$\frac{A + B}{2} + \frac{\kappa}{4}(A + B)(A^2 + B^2) = P. \tag{16}$$

The left side increases with $B$ and brackets $P$ between $B = 0$ and $B = A$, so the cubic has exactly one root in $(0, A)$. The residual spread factor is $\beta_{\mathrm{res}} = 1 + B$, with $B = A$ for sticking and $B = 0$ for return. It is the residual radial extent of the model coordinate, not a measured wetted footprint: relating it to the area left wetted, or to the volume retained, would require a contact-line model that the radial coordinate does not contain.

The three outcomes are sketched in Fig. 2. They share the same spreading phase and part ways only after the first turning point, depending on what pinning allows. Each end state is also recorded by a different observable. A stuck drop keeps its maximum radial extent; an arrested drop stops at a smaller residual extent that reflects the inward pinning work; a returning drop reaches the reference extent with a measurable retraction speed. For this reason the inverse relations of Section 3.6 pair the maximum spread with $e_r$ on one branch and with $B$ on the other.

Two consequences follow when $P$ decreases with spacing ($\nu < 1$). First, $\beta_{\mathrm{res}}$ grows with spacing in the stick regime, because $A$ does, and then falls through the arrest regime to unity at $a_c$. Its maximum therefore occurs at the stick boundary,

$$\max_a \beta_{\mathrm{res}} = 1 + A_s(\kappa, H), \tag{17}$$

and its height does not depend on $D_e$, $|\cos\theta^*|$ or the edge exponent $\nu$, provided the spacing range crosses $P_s$. Second, the arrest window has a width in force and a width in spacing,

$$\frac{a_c}{a_s} = \left(\frac{P_s}{P_c}\right)^{1/(1-\nu)}, \qquad 2\sqrt{\tfrac{2}{3}} \;<\; \frac{P_s}{P_c} \;<\; 4\left(\tfrac{2}{5}\right)^{3/4}, \tag{18}$$

where $P_s/P_c$ depends on $\kappa H$ alone. The lower bound is reached in the linear-spring limit $\kappa H \to 0$, where $A_s^2 = 2H/3$ and $A_c^2 = H$, and the upper bound in the quartic-dominated limit $\kappa H \to \infty$, where $A_s^4 \to 4H/(5\kappa)$ and $A_c^4 \to 2H/\kappa$. We checked numerically that the ratio increases monotonically between these limits for $10^{-3} \le \kappa H \le 10^6$. These bounds apply to the force ratio. The spacing ratio $a_c/a_s$ equals $P_s/P_c$ only for the fixed-edge closure, $\nu = 0$; for $\nu > 0$ it is amplified by the exponent $1/(1-\nu)$. At baseline ($\kappa H = 27.5$) $P_s/P_c = 1.93$, and $a_c/a_s = 1.93$, 2.40, 3.72 and 13.87 for $\nu = 0$, 0.25, 0.5 and 0.75 (Fig. 12a). For $\nu = 1$ the force does not depend on spacing and no spacing boundaries exist. The spacing ratio is therefore independent of the edge-force magnitude $C$ at fixed $\nu$, but not of the scaling law itself. Conversely, if both boundaries are observed in a spacing series, the exponent follows from

$$\nu = 1 - \frac{\ln(P_s/P_c)}{\ln(a_c/a_s)}, \tag{19}$$

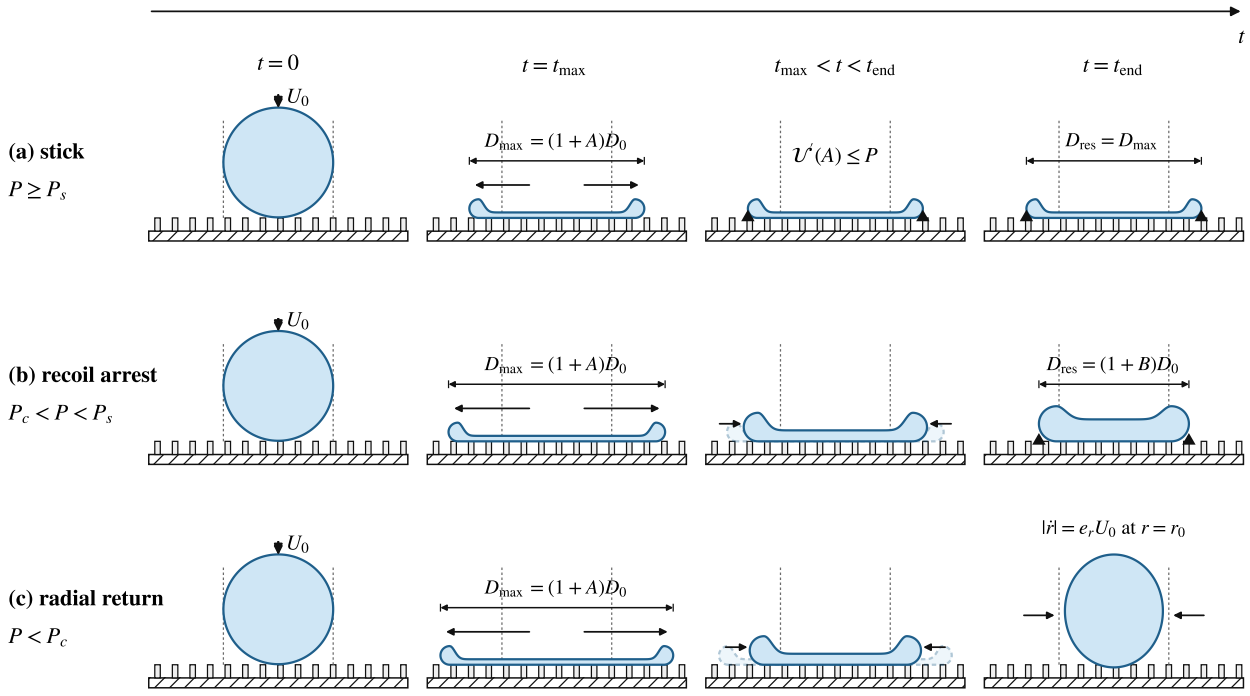


Figure 2: Side-view schematic of the first impact cycle in the three regimes. Columns show impact ($t = 0$), maximum spread ($t = t_{\max}$), the interval after maximum spread, and the end of the first cycle ($t = t_{\text{end}}$). Dashed vertical lines mark the reference extent $r = r_0$, and filled triangles mark pinned contact lines. (a) Stick, $P \geq P_s$: the restoring force at maximum spread cannot overcome pinning, $\mathcal{U}'(A) \leq P$, and the effective extent remains at $D_{\text{res}} = D_{\max} = (1+A)D_0$. (b) Recoil arrest, $P_c < P < P_s$: the drop recoils, but pinning work exhausts the stored energy before the reference extent is reached, and the contact line re-pins at $D_{\text{res}} = (1 + B)D_0$, with $B$ from equation (16). (c) Radial return, $P < P_c$: the drop passes the reference extent with radial speed $|\dot{r}| = e_r U_0$, equation (13). In (b) and (c), faint outlines in the third column show the preceding maximum-spread shape. The rim–lamella profile follows side-view observations of impacting drops [2]. The drawing is qualitative, and texture and drop are not to scale. $D_{\text{res}}$ is the residual radial extent of the model coordinate, not a measured wetted diameter, and panel (c) does not imply detachment. The regime conditions hold for any edge-scaling exponent.

which turns the window into a test of the force-scaling law. In the same two limits $P_c$ scales as $\mathrm{We}^{1/2}$ and $\mathrm{We}^{3/4}$, so for any $\nu < 1$ the boundaries move to finer spacing as the impact energy increases.

The sticking condition assumes equal static and kinetic capacities. If the static capacity is $\sigma P$, sticking requires $\mathcal{U}'(A) \le \sigma P$, and the left relation in equation (15) becomes $\mathcal{U}(A_s) + A_s\mathcal{U}'(A_s)/\sigma = H$. The return boundary does not change. The factor $\sigma$ is also the natural place to separate a static pinning capacity, which hysteresis measures, from a larger kinetic resistance during motion (Section 5.8).

### 3.4 Phase-plane geometry of the three regimes

The thresholds have a direct geometric meaning in the phase plane $(x, x')$. On each leg the motion conserves the energy $\frac{1}{2}x'^2 + \mathcal{U}(x) \pm Px$, so trajectories are level curves of a tilted potential. The tilt changes sign with the direction of motion. With $x' > 0$ the friction term adds $+Px$; with $x' < 0$ it adds $-Px$. Every point of the segment

$$x' = 0, \qquad 0 \le x \le x_P, \qquad \mathcal{U}'(x_P) = P, \tag{20}$$

is an equilibrium, because the static reaction can balance the restoring force there. This sticking zone replaces the single equilibrium of a frictionless oscillator. A first-cycle outcome is then decided by where the trajectory meets the axis $x' = 0$. If the outward branch reaches the axis inside the sticking zone, $A \le x_P$, which is the condition $\mathcal{U}'(A) \le P$, and the drop sticks at maximum spread. If $A > x_P$, recoil begins, and the inward branch either meets the axis again at $x = B > 0$, which necessarily lies inside the zone, or reaches $x = 0$ with speed $e_r Q$ (Fig. 3).

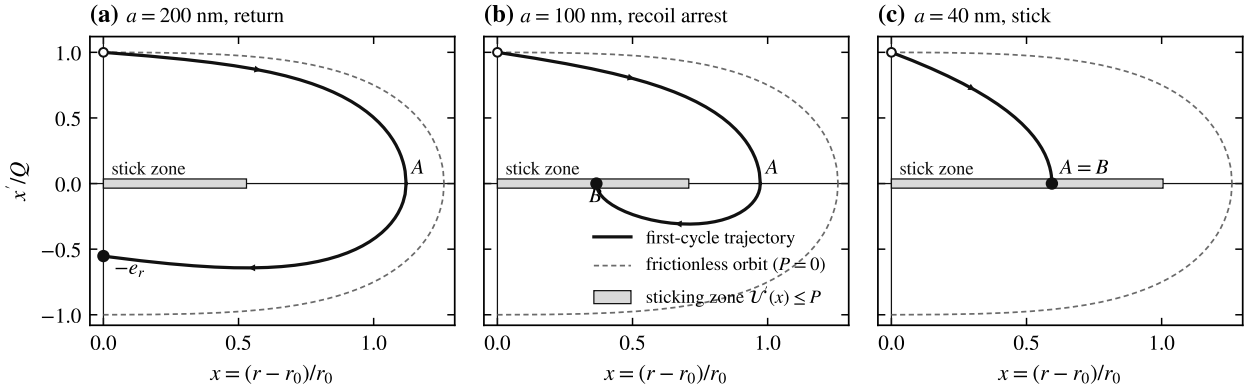


Figure 3: Exact first-cycle phase-plane trajectories of equation (2) in the saturated-pinning limit with $\zeta = 0$, at the baseline $\mathrm{We} = 18.3$ and $\kappa = 6$, for the fixed-edge closure. (a) $a = 200$ nm, $P = 1.42$: return with $e_r = 0.553$. (b) $a = 100$ nm, $P = 2.84$: recoil arrest at $B = 0.366$. (c) $a = 40$ nm, $P = 7.10$: sticking at maximum spread, $A = B = 0.594$. The solid curves are the outward ($x' > 0$) and inward ($x' < 0$) branches, and small arrowheads give the direction of motion. Open circles mark the impact state $(0, Q)$, and filled circles mark the end of the first cycle. The grey bar is the sticking zone of equation (20), whose half-width $x_P$ grows from 0.53 to 1.01 across the three cases. The dashed curve is the frictionless orbit, $P = 0$, for reference. The curves are computed, not sketched.

Figure 3 shows the three cases at the baseline Weber number. All three trajectories start from the same impact state, but the outward branch is pulled inside the frictionless orbit by the outward

pinning work $PA$. At $a = 200$ nm the turning point $A = 1.120$ lies well beyond the sticking zone ($x_P = 0.530$), and the inward branch reaches $x = 0$ with $e_r = 0.553$. At $a = 100$ nm, $A = 0.973$ still exceeds $x_P = 0.708$, so recoil starts, but the inward branch returns to the axis at $B = 0.366$, inside the zone. At $a = 40$ nm the sticking zone ($x_P = 1.005$) already contains the turning point $A = 0.594$, and no recoil occurs. The stick and return boundaries of equations (14) and (15) are therefore tangency conditions. The stick boundary is reached when the turning point touches the edge of the sticking zone, $A = x_P$. The return boundary is reached when the inward branch arrives at the origin with zero speed.

The linear limit $\kappa = 0$ makes the construction explicit and connects it to the classical Coulomb oscillator [14]. Each branch is then a circular arc centred at $x = \mp P$, so a half-cycle reflects the turning point about $x = P$. The recoil end point is $B = 2P - A$, which is equation (16) at $\kappa = 0$. Sticking at maximum spread requires $A \le P$, and return requires $A > 2P$. These are the familiar results that a Coulomb oscillator loses $2P$ of amplitude per half-cycle and stops inside a dead zone of half-width $P$. The quartic stiffness bends the arcs and moves the zone edge to $x_P < P$, but it leaves the construction unchanged. The phase plane also shows why the residual extent is non-monotonic in spacing. Decreasing $P$ moves the turning point outward but shrinks the sticking zone, and the residual extent is largest where the two meet.

### 3.5 Energy budget and exact sensitivities

For a returned trajectory,

$$H = K_{\mathrm{return}} + 2PA. \tag{21}$$

Pinning removes $PA$ on each leg, and the potential energy is zero on return to the reference. For arrest at $B \ge 0$ the budget is $H = \mathcal{U}(B) + P(2A - B)$, with $B = A$ for immediate sticking. The energy held in a pinned shape is therefore stored, not recovered as kinetic energy.

Implicit differentiation gives

$$A_P = -\frac{A}{\mathcal{U}'(A) + P}, \quad A_\kappa = -\frac{A^4}{4[\mathcal{U}'(A) + P]}, \quad A_H = \frac{1}{\mathcal{U}'(A) + P}. \tag{22}$$

For $\nu = 0$,

$$\frac{\partial \beta_{\max}^{(0)}}{\partial \ln a} = \frac{PA}{\mathcal{U}'(A) + P} > 0, \qquad \frac{\partial (e_r^{(0)})^2}{\partial P} = -\frac{2A\mathcal{U}'(A)}{H[\mathcal{U}'(A) + P]} < 0. \tag{23}$$

The fixed-edge solution therefore cannot show alternating peaks in spacing. All spacing sensitivities carry the factor $1 - \nu$ and vanish at $\nu = 1$. The leading-order results do not depend on $\alpha$, because viscosity has been left out on purpose. Near $e_r = 0$ the relative sensitivity of the recovery becomes ill-conditioned.

A measured maximum spread fixes only the combination $\mathcal{U}(A) + PA = H$, so it cannot separate stiffness from pinning. The edge scale and $|\cos\theta^*|$ also appear only as a product. Separating them requires further measurements.

### 3.6 Inverse identification from two observables

A second observable from the same impact closes the problem. On the return branch, the measured recovery $e_r$ and maximum spread $A = \beta_{\max} - 1$ give

$$P = \frac{H(1 - e_r^2)}{2A}, \qquad \kappa = \frac{4\left(H - \frac{1}{2}A^2 - PA\right)}{A^4}. \tag{24}$$

In the arrest regime the residual extent $B = \beta_{\mathrm{res}} - 1$ takes the place of $e_r$. Substituting equation (16) into the amplitude equation makes $\kappa$ appear linearly, and with $S = A + B$ and $q = A^2 + B^2$,

$$\kappa = \frac{H - \frac{1}{2}A^2 - \frac{1}{2}AS}{\frac{1}{4}A^4 + \frac{1}{4}ASq}, \qquad P = \frac{S}{2} + \frac{\kappa}{4}Sq. \tag{25}$$

In round-trip tests at $a = 80$, 100, 200 and 400 nm, both relations return the model parameters to machine precision. These tests confirm algebraic consistency only; Section 5.10 tests robustness to measurement noise. Under the fixed-edge closure the identified force then gives the product $D_e|\cos\theta^*| = 4aP/(3\pi)$. The return-branch estimate becomes ill-conditioned when recovery is strong, since $\partial \ln P / \partial \ln e_r = -2e_r^2/(1 - e_r^2)$; this factor is $-0.88$ at $a = 200$ nm and $-3.41$ at $a = 400$ nm. Pinning is therefore best identified from impacts in the arrest regime or close to the return boundary, and stiffness where pinning work is small. In practice, high-speed side-view imaging that resolves $\beta_{\max}$ together with either the retraction speed or the arrested radial extent, at two or more spacings, over-determines $\kappa$ and $C$ and so tests the closure itself.

### 3.7 Hysteresis-equivalent force and an admissibility bound

The classical retention force of a pinned contact line [15] gives $P$ a measurable meaning. If a resistance $\gamma(\cos\theta_r - \cos\theta_a)$ per unit length acts along the reference perimeter $2\pi r_0$, then $F_{\mathrm{pin}} = 2\pi r_0 \gamma\, \Delta\cos$ with $\Delta\cos = \cos\theta_r - \cos\theta_a$. Dividing by $kr_0 = 4\pi\gamma r_0/3$ gives

$$P = \tfrac{3}{2}\,\Delta\cos, \qquad \Delta\cos_c = \tfrac{2}{3}P_c(\kappa, \mathrm{We}), \qquad \Delta\cos_s = \tfrac{2}{3}P_s(\kappa, \mathrm{We}). \tag{26}$$

Surface tension cancels, so the regime thresholds become wetting thresholds that depend only on $\kappa$ and We. Since $\Delta\cos \le 2$ for any pair of contact angles, hysteresis can supply at most $P = 3$. A geometric closure that predicts $P > 3$ therefore needs some resistance beyond contact-angle hysteresis on the reference perimeter, for example adhesion after impalement or a longer effective contact line. For the fixed-edge closure, $P = C/a \le 3$ requires

$$a \ge a_{\mathrm{adm}} = \frac{C}{3} = \frac{\pi}{4}D_{e,r}|\cos\theta^*|. \tag{27}$$

The bound does not depend on the impact conditions. It tests whether the encounter-density closure is consistent with the hysteresis interpretation; it does not imply that finer textures cannot exist.

Three quantities must be kept apart when this relation is used. The static apparent angle $\theta^*$ characterizes a drop at rest and does not by itself fix any force. The quasi-static hysteresis $\theta_a - \theta_r$ is measured by slowly adding liquid to and withdrawing it from a sessile drop through a needle, or from the angles at the onset of sliding on a tilting plate, and it gives the static pinning capacity. Dynamic contact-line resistance depends on contact-line speed and can be obtained from the dynamic angles recorded by high-speed imaging during spreading and retraction. Equation (26) uses the quasi-static hysteresis and therefore describes a static capacity. Applying it along the reference perimeter $2\pi r_0$ is appropriate when the contact line moves as a whole, at low capillary number, in a stable Cassie state and at moderate deformation. At maximum spread the perimeter is larger by the factor $1 + A$, which raises the hysteresis force by at most that factor, about 2.3 at baseline.

# 4 Weak-viscosity extension and verification

## 4.1 First-order energy correction

Along the zero-viscosity trajectory define

$$I_o = \int_0^A \sqrt{2[H - \mathcal{U}(x) - Px]}\, dx, \tag{28}$$

$$I_i = \int_0^A \sqrt{2[\mathcal{U}(A) - \mathcal{U}(x) - P(A - x)]}\, dx. \tag{29}$$

$I_i$ is needed only when the drop returns. Since the viscous work is $2\zeta \int x'^2 ds = 2\zeta \int |x'|\, |dx|$, the first-order amplitude is

$$A_\zeta = A - \frac{2\zeta I_o}{\mathcal{U}'(A) + P} + O(\zeta^2). \tag{30}$$

Accounting for both the viscous work and the shorter pinning path gives

$$K_{\mathrm{return},\zeta} = H - 2PA - 2\zeta(I_o + I_i) + \frac{4\zeta P I_o}{\mathcal{U}'(A) + P} + O(\zeta^2). \tag{31}$$

The last term matters: damping reduces the spread and therefore also the pinning work. On a branch well away from arrest, $e_{r,\zeta} = \sqrt{K_{\mathrm{return},\zeta}/H}$. The expansion is not uniform as the leading-order return energy approaches zero, and clipping a negative first-order energy does not define a finite-viscosity boundary; equation (14) remains a zero-viscosity result.

The sensitivity to the width-to-pitch ratio follows as

$$\frac{\partial \beta_{\max}}{\partial \alpha} = -\frac{4\zeta_0 \alpha I_o}{\sqrt{\mathrm{Re}}[\mathcal{U}'(A) + P]} + O(\zeta^2). \tag{32}$$

It is negative under this closure. Over the ratio range $\zeta$ stays between 0.0153 and 0.0207, so this is a small-damping result rather than a general statement about wall morphology.

## 4.2 Evaluation and independent verification

We evaluate the analytical expressions on a $361 \times 61$ grid by bracketed root finding and adaptive quadrature. The transition itself is computed from equation (14) and does not depend on the grid. The root tolerance is $10^{-14}$, the absolute and relative quadrature tolerances are $10^{-10}$, and refinement from $10^{-8}$ to $10^{-12}$ was checked at seven spacings.

As an independent check, we integrated the piecewise ODEs at $a = 40$, 65, 100, 150, 200, 300 and 400 nm, using the appropriate constant-force sign on each leg together with reversal, stopping and return events. The relative and absolute tolerances were $2 \times 10^{-11}$ and $10^{-12}$, with a maximum dimensionless step of 0.01. The zero-viscosity amplitude and recovery agree to better than $10^{-8}$ and $10^{-7}$, respectively. At $\alpha = 0.30$ the largest first-order spread discrepancy is $4.25 \times 10^{-5}$, and the largest recovery discrepancy among the four returning cases is 0.00111. Quadrature refinement changes the spread correction by less than $10^{-12}$. These figures measure numerical and approximation error, not physical validity, and we make no accuracy claim for the recovery arbitrarily close to the return boundary. The ODE runs verify the analysis; they do not replace it.

These evaluations use the ideal saturated resistance rather than a finite smoothing $\epsilon$, so no new claim is made about convergence in the smoothing speed. Refining an analytical plot cannot, of course, validate the geometry closure or physical rebound.

# 5 Results and parametric analysis

## 5.1 Spacing under the fixed-edge closure

Table 2: Geometry study for the fixed-edge closure ($\nu = 0$) at baseline. $\beta_{\max}^{(0)}$, $e_r^{(0)}$ and $\beta_{\mathrm{res}}^{(0)}$ are exact zero-viscosity values; the first-order spread is the weak-viscosity approximation at $\alpha = 0.30$. Values are given to four decimals so that they can be checked; their physical uncertainty is governed by the closure and is much larger.

| $a$ (nm) | $P$ | $\beta_{\max}^{(0)}$ | $\beta_{\max}$, first order | $e_r^{(0)}$ | $\beta_{\mathrm{res}}^{(0)}$ | Regime |
|---|---|---|---|---|---|---|
| 40 | 7.100 | 1.5939 | 1.5893 | 0.0000 | 1.5939 | stick |
| 65 | 4.369 | 1.8179 | 1.8110 | 0.0000 | 1.8179 | stick |
| 100 | 2.840 | 1.9728 | 1.9650 | 0.0000 | 1.3663 | arrest |
| 150 | 1.893 | 2.0714 | 2.0633 | 0.3377 | 1.0000 | return |
| 200 | 1.420 | 2.1201 | 2.1119 | 0.5526 | 1.0000 | return |
| 300 | 0.947 | 2.1680 | 2.1598 | 0.7191 | 1.0000 | return |
| 400 | 0.710 | 2.1915 | 2.1833 | 0.7941 | 1.0000 | return |

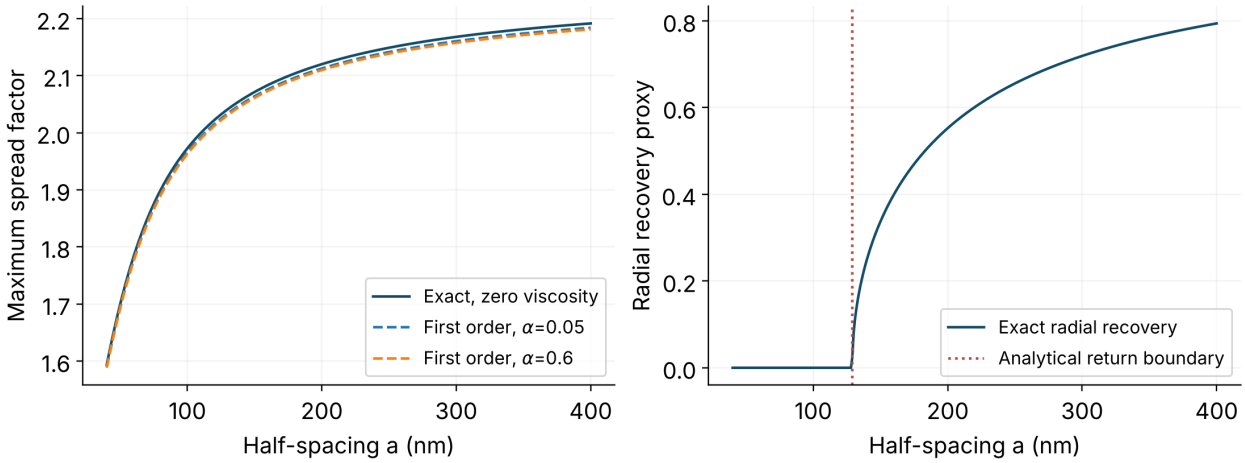


Figure 4: Spacing response for the fixed-edge closure ($\nu = 0$) at baseline. Left: exact zero-viscosity maximum spread and first-order weak-viscosity spread for $\alpha = 0.05$ and 0.6. Right: exact zero-viscosity radial recovery; the dotted line is the analytical return boundary of equation (14), not an inferred contour feature.

At baseline, $Q = 3.02636$, $H = 4.57942$, $A_c = 1.03924$ and $P_c = 2.20325$. With $C = 284.0$ nm the fixed-edge return boundary is $a_c \approx 129$ nm, a pitch of about 258 nm. Dimensionless model quantities such as $A_c$ and $P_c$ are quoted to several digits because they are exact evaluations of the stated model. Spacings are rounded, because their physical uncertainty is set by the closure and is far larger than the computational precision: a factor-of-two change in $C$ moves them by a factor of two. Across the spacing interval the exact maximum spread rises from 1.594 to 2.192, a 37.5% increase in effective diameter and an 89% increase in the corresponding area. At 400 nm the radial recovery is 0.7941, so a fraction 0.6305 of the generalized kinetic energy is recovered. At small spacing the recovery is zero because the drop arrests before it can return. On the returning branch

it increases with spacing, as equation (23) requires, because the combined outward and inward pinning work falls as the spacing grows.

All edge-exponent scenarios share the reference pinning force of [13] at $a = 65$ nm, so differences at other spacings reflect extrapolation of the closure rather than a different reference force. The analytical and weak-viscosity values need not match exactly the finite-smoothing calculation of [13], which used a numerical capture band.

### 5.2 Ratio dependence and force-scale uncertainty

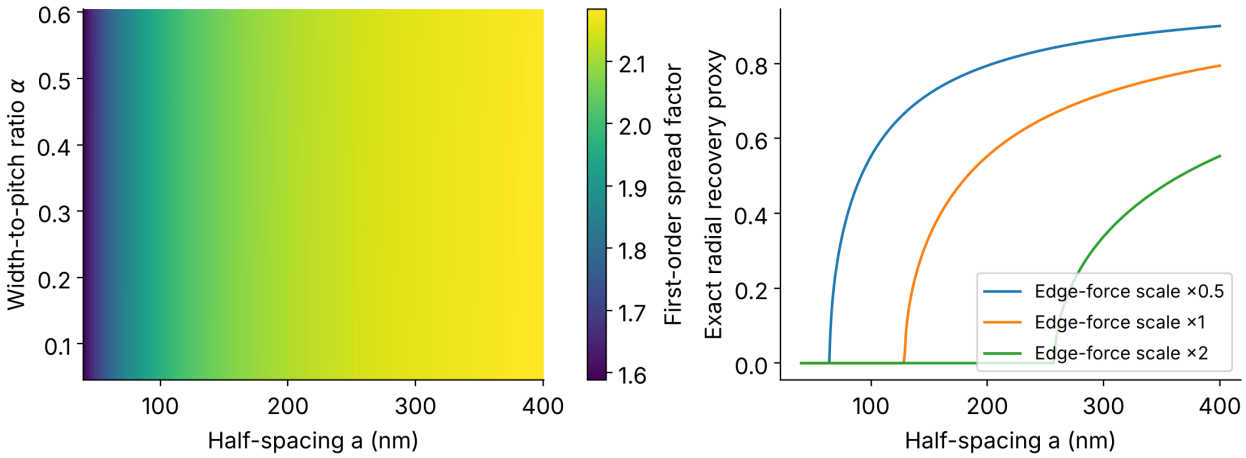


Figure 5: Fixed-edge closure ($\nu = 0$) at baseline. Left: first-order weak-viscosity spread over spacing and width-to-pitch ratio. Right: exact zero-viscosity radial recovery for edge-force multipliers 0.5, 1 and 2. These are deterministic force-scale scenarios, not statistical confidence bounds.

The width-to-pitch ratio acts only through a small viscous correction. Although $\phi$ varies by a factor of 144, the damping factor $1+\phi$ changes only from 1.0025 to 1.36. At 400 nm, raising $\alpha$ from 0.05 to 0.60 lowers the first-order maximum spread by 0.00270, about 0.12%. This weak effect is a consequence of the closure and should not be taken as a general insensitivity to wall morphology; height, flexibility, network topology and wetting transitions were not tested. In the present closure the solid fraction enters only the damping. In reality a change of $\phi$ would also change the pinning, through the length of wall top under the contact line, the capillary pressure that resists impalement, and possibly the wetting state, so the small predicted width effect is conditional on leaving those effects out.

Multiplying the edge force by a constant scales $P$ and the fixed-edge boundary spacing alike. Halving or doubling it moves $a_c$ to about 64 or 258 nm, so any plotted boundary is conditional on the assumed edge scale. Without fabrication constraints and further design objectives, no optimum spacing follows.

### 5.3 Alternative geometry scaling

The $\nu = 1/2$ family responds more weakly than the fixed-edge family, and for $\nu = 1$ the outputs are constant at fixed ratio and impact conditions. For $\nu > 1$ the sensitivities would change sign, because resistance would then increase with spacing. The inferred trend is therefore controlled by the structural assumption about geometry, which is also why the spacing width of the arrest window grows rapidly with $\nu$ (Section 3).

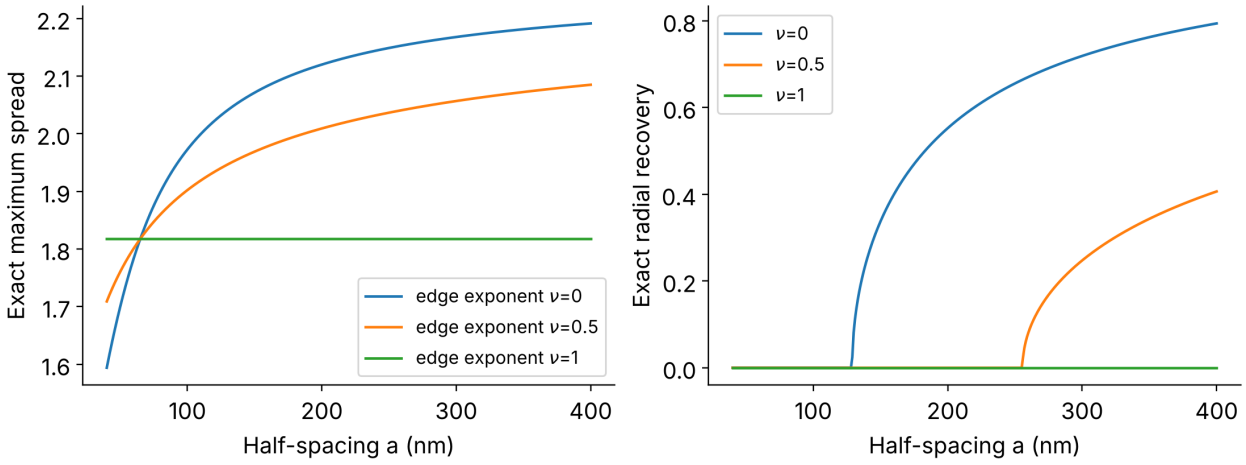


Figure 6: Exact zero-viscosity maximum spread (left) and radial recovery (right) at baseline for $\nu = 0$, 0.5 and 1, all matched to the reference force at $a_r = 65$ nm. Proportional edge scaling ($\nu = 1$) eliminates the spacing dependence. Scenario comparison, not a fit.

### 5.4 Three regimes and the residual radial extent

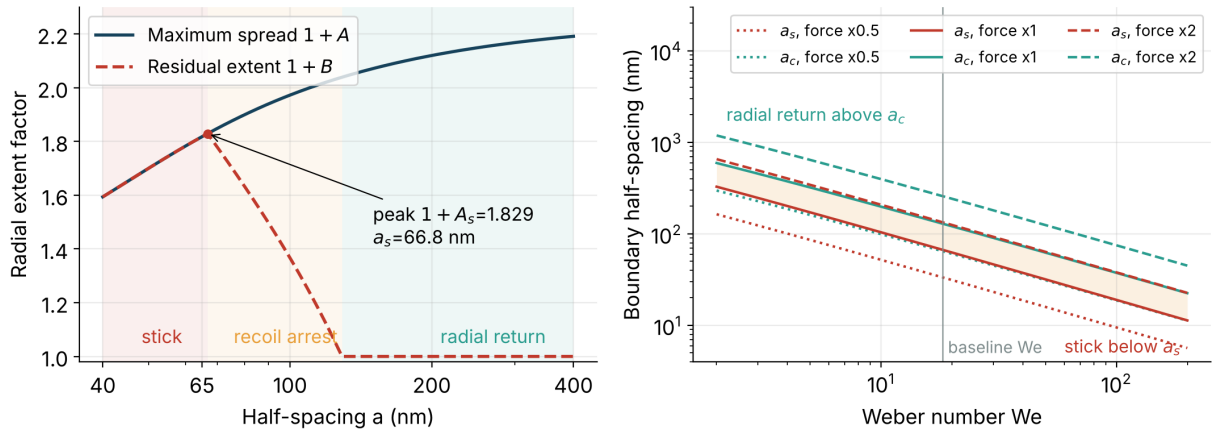


Figure 7: Exact zero-viscosity results for the fixed-edge closure ($\nu = 0$). Left: maximum spread and residual radial extent at baseline, with the stick, recoil-arrest and radial-return regimes from equations (14) and (15). The residual extent peaks at the stick boundary. Right: stick ($a_s$) and return ($a_c$) boundaries against Weber number for edge-force multipliers 0.5, 1 and 2; the shaded band is the baseline arrest window. Boundary positions are closure-scenario predictions.

At baseline, equation (15) gives $A_s = 0.82932$ and $P_s = 4.25165$, which places the fixed-edge stick boundary at $a_s \approx 67$ nm (pitch about 134 nm). The spacing range thus contains all three regimes: drops stick at maximum spread below about 67 nm, recoil and arrest between about 67 and 129 nm, and return at larger spacing (Fig. 7). The maximum spread increases monotonically throughout. The residual extent, by contrast, rises to $\beta_{\mathrm{res}} = 1.829$ at $a_s$ and then falls back to unity at $a_c$, passing 1.366 at 100 nm. Independent piecewise ODE integrations reproduce the residual extent to within $10^{-11}$ at seven spacings spanning the three regimes.

For $\nu = 0$ the spacing ratio of the arrest window equals the force ratio, $a_c/a_s = P_s/P_c = 1.930$ at

$\kappa H = 27.5$, within the bounds of equation (18); for other exponents it is larger (Fig. 12a). Halving or doubling the edge force moves the stick boundary to about 33 or 134 nm and the return boundary to about 64 or 258 nm, but leaves both the ratio and the peak residual extent unchanged. The right panel of Fig. 7 shows both boundaries moving to finer spacing as the Weber number increases. On logarithmic axes their slopes approach $-3/4$ at high We, so a texture that arrests a slow impact may allow radial return at a higher impact speed.

### 5.5 Global sensitivity to uncertain inputs

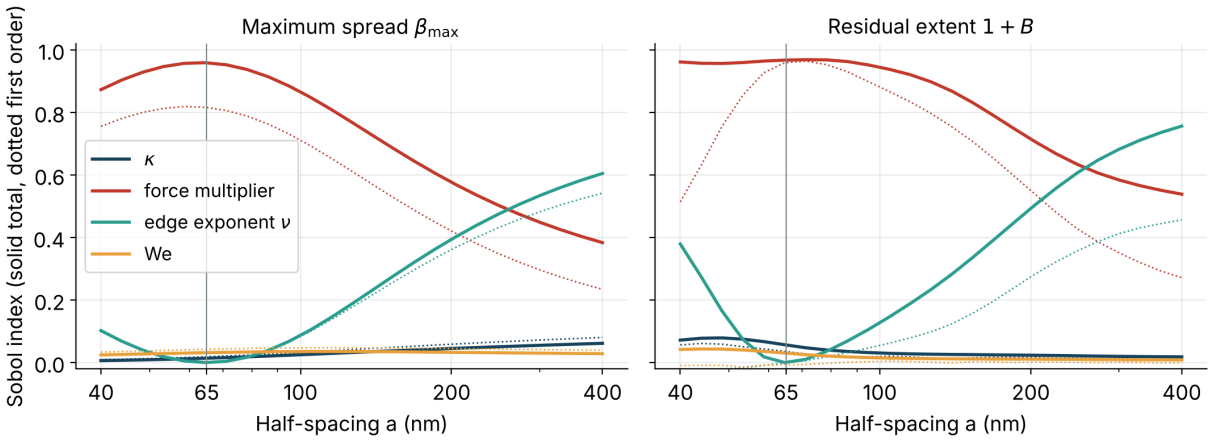


Figure 8: Total-effect (solid) and first-order (dotted) Sobol indices of maximum spread and residual extent. Inputs are uniformly distributed: $\kappa \in [4, 8]$, log edge-force multiplier in $[\ln 0.5, \ln 2]$, $\nu \in [0, 1]$, and We within $\pm 10\%$ of baseline. These are exploratory uniform scenario ranges, not calibrated distributions. Exact zero-viscosity outputs. The vertical line marks the reference spacing $a_r$, where $\nu$ has no effect.

Local derivatives describe sensitivity at a single parameter set. To rank the uncertain inputs jointly we computed first-order and total Sobol indices with the Saltelli and Jansen estimators [16], using $N = 2^{15}$ base samples per spacing and therefore $6N$ evaluations of the exact solution. Doubling $N$ changed no index by more than 0.013. The ranges listed in the caption of Fig. 8 are scenario ranges, not calibrated probability distributions.

For the maximum spread, the edge-force multiplier explains at least 75% of the variance for $a \leq 130$ nm, with a largest total index of 0.96 at the reference spacing. Above about 260 nm the edge-scaling exponent takes over, reaching a total index of 0.61 at 400 nm. The stiffness and Weber-number uncertainties stay below 0.07 everywhere. The residual extent behaves similarly, except that below about 60 nm its total indices clearly exceed the first-order ones. This points to interactions between inputs: because the regime can switch, the effect of $\nu$ there depends on the force scale. In practical terms, at fine spacing a measurement of the edge-force magnitude is worth more than a better stiffness calibration, whereas at coarse spacing the main unknown is how edge resistance scales with pitch. This ranking belongs to the stated ranges, which are exploratory scenarios rather than empirically calibrated distributions. Different ranges would change it. To first order, the variance share of an input scales with the variance of its range times the square of the output sensitivity, so narrowing the edge-force range from a factor of two to a factor of 1.25 would reduce that input's contribution roughly tenfold, by $(\ln 1.25/\ln 2)^2 \approx 0.10$, and would pass the leading rank at fine spacing to $\nu$ or $\kappa$. If the pinning force were as small as the measured hysteresis

of [12] suggests (Section 5.8), the edge-force inputs would lose almost all influence on the maximum spread, and the stiffness and the energy projection would dominate. The indices should therefore be recomputed once measured parameter distributions are available.

### 5.6 Benchmark against maximum-spread correlations

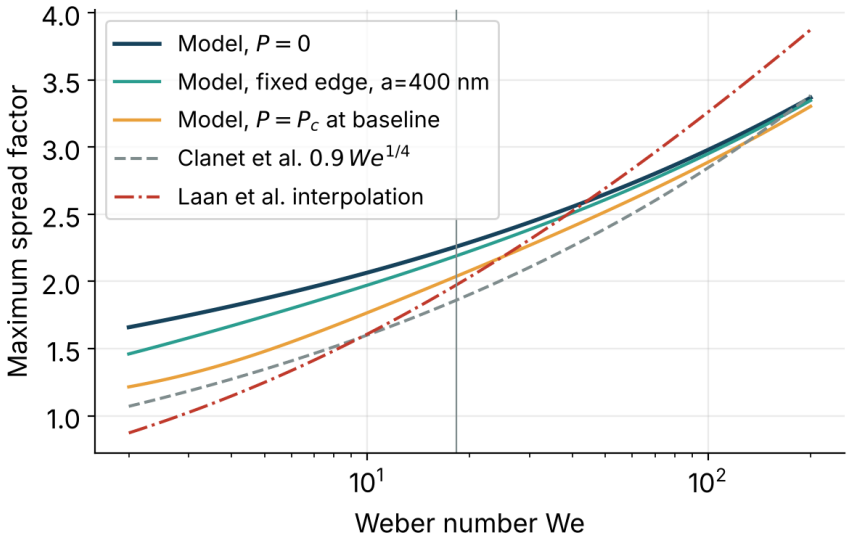


Figure 9: Model maximum spread against the inertia–capillary scaling of Clanet et al. [2] and the interpolation of Laan et al. [17] for water drops of the baseline size. Exact zero-viscosity model curves use $\kappa = 6$ with $P = 0$, with the fixed-edge ($\nu = 0$) force at 400 nm, and with $P = P_c$ at baseline.

Correlations from impact experiments on smooth surfaces provide an external check on the inherited stiffness calibration, although not on the texture effects. At the baseline Weber number the frictionless model gives $\beta_{\max} = 2.26$, compared with 1.86 from $0.9\,\mathrm{We}^{1/4}$ [2] and 1.98 from the interpolation of Laan et al. [17]. Pinning on the textured baseline brings the model closer to these values. The local exponent $d\ln(\beta_{\max} - 1)/d\ln \mathrm{We}$ of the frictionless model is 0.257 at $\mathrm{We} = 200$, as expected in the quartic limit. The overprediction is largest at low Weber number, where the linear spring term and the projection of all incident energy onto the radial coordinate dominate (Fig. 9). The comparison supports the asymptotic scaling but also shows that $\kappa = 6$, calibrated in [13], should be recalibrated before it is used at other impact speeds; Section 5.11 shows how a different $\kappa$ moves the thresholds.

### 5.7 Wetting thresholds and closure admissibility

At baseline, equation (26) gives $\Delta\cos_c = 1.469$ and $\Delta\cos_s = 2.834$. The return threshold corresponds to a high but attainable hysteresis, whereas the stick threshold exceeds the physical limit, so hysteresis alone cannot hold a baseline impact at maximum spread. The left panel of Fig. 10 shows that sticking by hysteresis is possible only for $\mathrm{We} < 11.4$. For hysteresis typical of superhydrophobic surfaces, radial return is predicted above $\mathrm{We} = 0.30$ for $\Delta\cos = 0.1$, above 1.83 for $\Delta\cos = 0.3$ and above 3.93 for $\Delta\cos = 0.5$, and recoil arrest occupies a band spanning a factor of

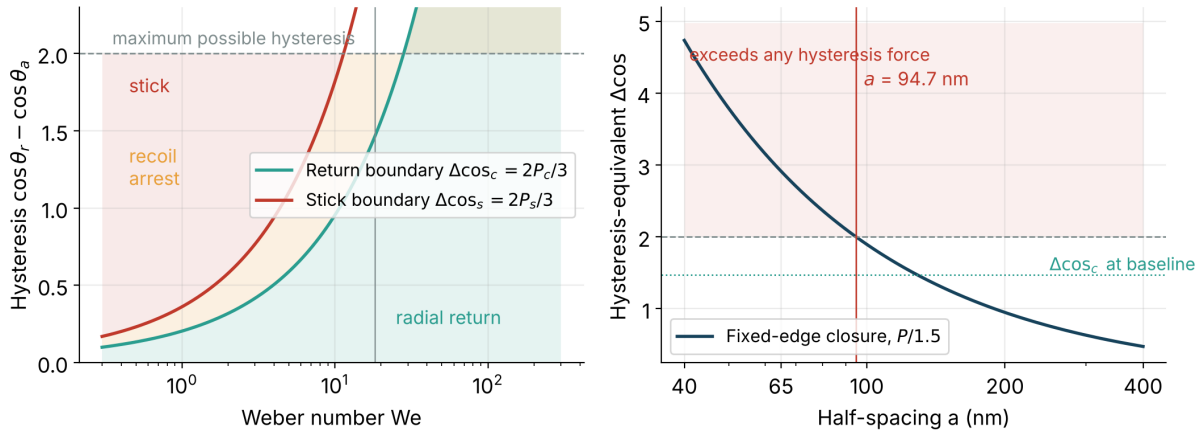


Figure 10: Left: first-cycle regimes in the plane of Weber number and contact-angle hysteresis from equation (26), with $\kappa = 6$. The dashed line is the upper limit $\Delta\cos = 2$. Right: hysteresis-equivalent force of the fixed-edge closure at baseline; values above 2 cannot be supplied by hysteresis on the reference perimeter, giving the admissibility bound of equation (27). Analytical zero-viscosity thresholds with $\kappa = 6$; the right panel uses $\nu = 0$ and the baseline edge scale.

about 2.4–2.6 in We. These thresholds agree with the experimental finding that the receding angle and hysteresis decide whether impacting drops recoil or remain deposited [18], and they do so with no fitted parameter other than $\kappa$.

For the baseline edge scale the admissibility bound is $a_{\mathrm{adm}} \approx 95$ nm. The reference force itself, $P = 4.37$ at $a_r = 65$ nm, corresponds to $\Delta\cos \approx 2.91$, which no pair of contact angles can produce. The whole baseline stick regime (below about 67 nm) and the finer part of the arrest regime therefore require more pinning force than hysteresis can provide (Fig. 10, right). There are two possible readings. Either the response at fine spacing involves additional resistance, as liquid penetration into nanowalls [12] and impalement transitions [7] would suggest, or the effective edge scale $D_{e,r} = 130$ nm overestimates the force at fine spacing. In both cases the predicted baseline stick regime cannot be attributed to contact-line hysteresis, and this conclusion follows from the closure itself without additional fitting.

### 5.8 Comparison with the measured wetting of nanowall surfaces

Yilbas et al. [12] report for their nanowall surfaces a static apparent angle of $158° \pm 2°$ and a contact-angle hysteresis of about 4° (given as $\pm 1°$ in the abstract and $\pm 2°$ in the text); the advancing and receding angles are not given separately. Taking $\theta_{a,r} = \theta^* \pm \Delta\theta/2$, the cosine hysteresis is $\Delta\cos \approx 0.026$ and equation (26) gives $P_{\mathrm{hys}} \approx 0.039$, with a range of 0.018–0.064 for $\theta^* = 156$–$160°$ and $\Delta\theta = 2$–$6°$. Even counted on the maximum-spread perimeter, the hysteresis force stays below 0.1. The closure value at the reference spacing of the same surfaces, $P = 4.37$, is about 110 times larger.

The two values lead to opposite first-cycle outcomes. The impact conditions of [12], drops of 10–30 $\mu$L released from 10–30 mm, span We ≈ 7–31. With $P_{\mathrm{hys}}$ every one of these nine conditions lies deep in the radial-return regime, with $e_r$ between 0.98 and 0.99 and a maximum spread essentially equal to the frictionless value ($\beta_{\max} = 2.26$ at baseline). With the closure value the model predicts sticking at maximum spread for We $\leq 18.3$ and recoil arrest at the higher speeds, so that no impact would return. Yilbas et al. observed rebound on these surfaces and reported restitution coefficients

that fall off only beyond We $\approx 30$, where the drops begin to break up. Within the model, the measured hysteresis is therefore consistent with the observations and the inherited closure is not.

This comparison clarifies what the closure represents. As calibrated in [13], the force reproduces a reduced maximum spread, so it lumps all resistance acting during spreading: dynamic contact-line dissipation, the viscous loss in the rim that the weak damping term underestimates, and any penetration of liquid into the texture. It should not be read as a static pinning force. Writing the resistance as $P = P_{\mathrm{hys}} + P_{\mathrm{dyn}}$, with $P_{\mathrm{hys}}$ from the measured angles and $P_{\mathrm{dyn}}$ the remainder, and applying only the static part to the sticking test ($\sigma = P_{\mathrm{hys}}/P$ in Section 3) is the consistent way to combine the two. With $\sigma \ll 1$, however, the motion must be followed beyond the first turning point, and $P_{\mathrm{dyn}}$ has not been measured. We therefore distinguish clearly between the closure, used here as a theoretical device that generates spacing-dependent scenarios, and a force law calibrated against wetting data, which does not yet exist for these surfaces. The spacing boundaries reported in this paper are predictions of that closure, not validated physical thresholds. The force thresholds $P_c$ and $P_s$ and their hysteresis forms, by contrast, do not depend on the closure and can be tested directly.

A quantitative comparison of maximum spread, spreading and recoil times and retraction with [12] would require the measured time histories, which that paper presents only graphically. We have not digitized them, because the energy projection and the stiffness calibration (Section 5.11) would have to be fixed by the same data first, leaving no independent test. One qualitative point already follows: with $P_{\mathrm{hys}}$ alone the model predicts nearly frictionless spreading, so the reduced spreading that [12] found on the nanowall surface, the smallest among the surfaces they tested, must come from the dynamic resistance that the closure lumps into $P$, or from damping stronger than the present weak-viscosity term.

### 5.9 Energy partition and radial timescales

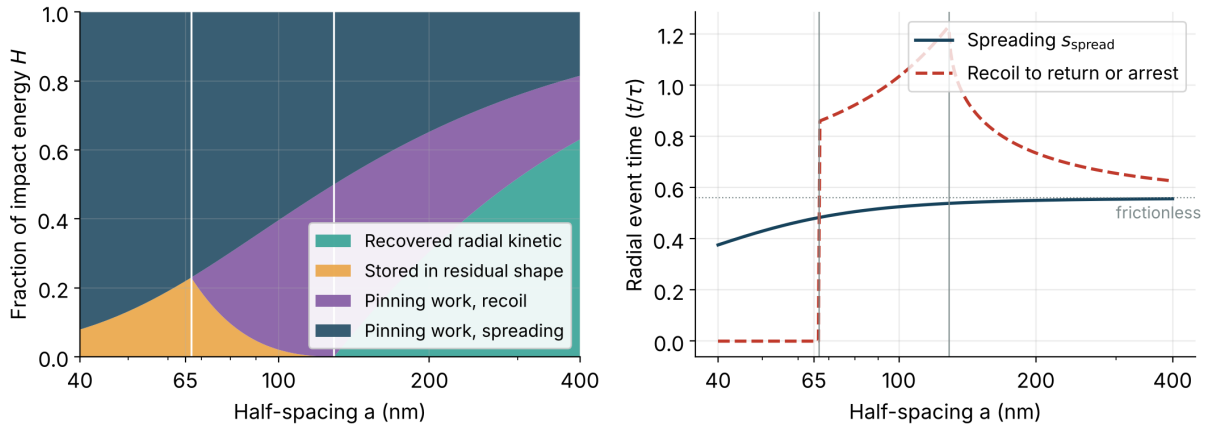


Figure 11: Exact zero-viscosity results for the fixed-edge closure ($\nu = 0$) at baseline. Left: first-cycle partition of the impact energy $H$; white lines mark $a_s$ and $a_c$. Right: radial spreading time and recoil time (to reference return or arrest) in units of $\tau = 8.135$ ms; vertical lines mark $a_s$ and $a_c$.

Figure 11 splits the impact energy into outward pinning work $PA$, inward pinning work $P(A-B)$, stored deformation energy $\mathcal{U}(B)$ and recovered kinetic energy; the four parts sum to $H$ within $10^{-9}$ at every sample. In the stick regime the stored share rises from 7.9% at 40 nm to a maximum of 23.0% at $a_s$. Through the arrest regime it falls to zero while the inward pinning work grows. At

$a_c$ the pinning work is the same on both legs, and together the two legs dissipate all of the impact energy. Beyond $a_c$ the recovered fraction grows to 63.1% at 400 nm. The stored-energy maximum coincides with the peak of the residual radial extent, so both mark the same stick boundary.

The quadratures of Section 3.1 give the radial event times directly. Without friction the spreading time is $0.560\tau$ (4.55 ms), much shorter than the linear-spring quarter period $\pi\tau/2$, so at this Weber number the quartic stiffness, rather than the linear term, sets the spreading duration. Pinning shortens spreading only modestly, to $0.376\tau$ at 40 nm, but lengthens recoil considerably. The recoil time rises through the arrest regime and peaks at the return boundary at $1.230\tau$ (10.0 ms), 2.2 times its frictionless value, before relaxing toward $0.626\tau$ at 400 nm on the returning branch. A recoil-to-spreading time ratio near 2.3 is therefore a timing signature of the return transition that high-speed imaging alone can detect, and measured retraction rates on non-wetting surfaces [19] provide a direct point of comparison. Independent ODE integrations reproduce both times within $10^{-11}$ at four spacings.

For comparison, the frictionless radial round trip takes $1.12\tau$, while bouncing water drops on superhydrophobic surfaces stay in contact for about $2.6\sqrt{\rho r_0^3/\gamma} = 2.6\tau$ [20]. The two times describe different events. Radial return is the passage of the effective coordinate through its reference value, whereas the contact time ends with detachment, after retraction has continued below the reference extent and the drop has lifted off. Their ratio is therefore not a contact-time relationship, and only a measured radius history on a given surface could relate the radial return to detachment.

## 5.10 Robustness of the inverse identification

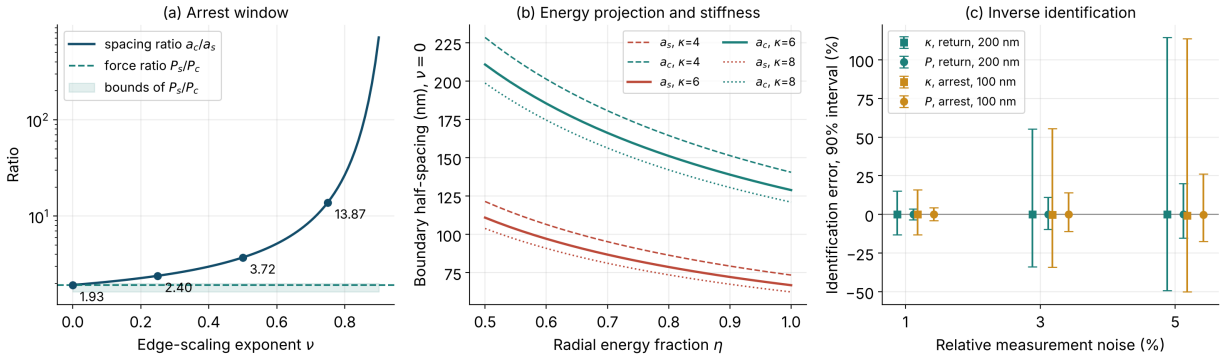


Figure 12: Robustness analyses of the exact zero-viscosity model at baseline. (a) Spacing ratio of the arrest window, $a_c/a_s = (P_s/P_c)^{1/(1-\nu)}$, against the edge-scaling exponent $\nu$; the dashed line is the force ratio $P_s/P_c$, whose bounds (shaded) hold for every $\nu$. (b) Fixed-edge ($\nu = 0$) stick and return boundaries against the fraction $\eta$ of impact energy assigned to radial motion, for $\kappa = 4$, 6 and 8. (c) Median and 90% interval of the relative error in $\kappa$ and $P$ identified from noisy synthetic observations (Monte Carlo, 40 000 samples per point), for a returning case at 200 nm and an arrested case at 100 nm, $\nu = 0$.

The round-trip tests of Section 3.6 use noise-free data from the model itself. To test practical identifiability we perturbed $\beta_{\max}$ and either $e_r$ (the retraction-speed ratio) or $\beta_{\text{res}}$ by independent Gaussian relative errors with standard deviations of 1, 3 and 5%, drew 40 000 samples per case and inverted each sample with equations (24) and (25). Table 3 and Fig. 12c summarize the results. Medians are unbiased to within 1.4%. The pinning force is well conditioned: its interval grows roughly in proportion to the noise and is narrowest near the return boundary, as the factor

$\partial \ln P / \partial \ln e_r$ predicts, so at 400 nm, where recovery is strong, it is about twice as wide as at 200 nm. The stiffness is poorly conditioned, because it comes from the small residual $H - \frac{1}{2}A^2 - PA$ divided by $A^4$. At 3% noise its interval already spans about $-34\%$ to $+56\%$, and at 5% the upper tail exceeds $+100\%$. Non-physical solutions ($\kappa \le 0$, or $\beta_{\mathrm{res}}$ outside $(1, \beta_{\max})$) do not occur at 1 and 3% and affect about 2% of arrest-regime samples at 5%.

Table 3: 90% intervals of the relative error (%) in the identified stiffness and pinning force for Gaussian relative noise of standard deviation $\varepsilon$ on both observables. Fixed-edge closure ($\nu = 0$), baseline impact, exact zero-viscosity model; Monte Carlo with 40 000 samples.

| | $\varepsilon = 1\%$ | | $\varepsilon = 3\%$ | | $\varepsilon = 5\%$ | |
|---|---|---|---|---|---|---|
| Case (observables) | $\kappa$ | $P$ | $\kappa$ | $P$ | $\kappa$ | $P$ |
| Return, 200 nm ($\beta_{\max}$, $e_r$) | $-13$, $+15$ | $-3$, $+4$ | $-34$, $+55$ | $-10$, $+11$ | $-49$, $+114$ | $-15$, $+20$ |
| Return, 400 nm ($\beta_{\max}$, $e_r$) | $-13$, $+15$ | $-6$, $+6$ | $-33$, $+52$ | $-19$, $+20$ | $-48$, $+107$ | $-31$, $+34$ |
| Arrest, 100 nm ($\beta_{\max}$, $\beta_{\mathrm{res}}$) | $-13$, $+16$ | $-4$, $+4$ | $-34$, $+56$ | $-11$, $+14$ | $-50$, $+114$ | $-18$, $+26$ |

Near the boundaries the identified pair can place an impact in the wrong regime. At 70 nm, just inside the arrest regime, 18% of samples at 3% noise and 30% at 5% are reclassified as sticking; at 125 nm, just inside the return boundary, 6% and 17% are reclassified as returning. On the return branch the identification is self-consistent by construction, because a measured $e_r > 0$ always yields return, and no misclassification occurred at 135 or 150 nm. Regime assignments within a few nanometres of a boundary, or from data with errors above about 3%, should therefore be reported with their probabilities.

We also tested prediction across impact speeds. Parameters identified at the baseline $\mathrm{We} = 18.3$ from the return-branch observables at 200 nm, with 3% noise, were used to predict a second impact at the same spacing. At $\mathrm{We} = 30$ the predicted $\beta_{\max}$ is 2.33 (90% interval 2.21–2.46; true value 2.33) and $e_r$ is 0.70 (0.69–0.72; true 0.70). At $\mathrm{We} = 10$, where the impact lies just inside the return regime (true $e_r = 0.083$), $\beta_{\max}$ is still predicted well (1.88; 1.80–1.95; true 1.87), but 39% of the parameter samples predict recoil arrest instead of return. Cross-speed prediction thus works away from the boundaries and inherits their ill-conditioning near them. With real data the same test would also check the model, since an error in the energy projection or the stiffness would appear as a speed-dependent bias that synthetic data cannot reveal.

### 5.11 Energy projection and stiffness

The initial condition assigns all of the incident kinetic energy to the radial coordinate. In reality part of it goes into vertical deformation, internal circulation and viscous loss in the impact region. We represent this by a fraction $\eta$ of the impact energy, $H = \eta \mathrm{We}/4$, and repeat the threshold analysis for $0.5 \le \eta \le 1$ (Fig. 12b). Lowering $\eta$ to 0.5 moves the fixed-edge stick and return boundaries outward from about 67 and 129 nm to about 111 and 211 nm, lowers the frictionless maximum spread from 2.26 to 2.04, and lowers the peak residual extent from 1.83 to 1.68. The force ratio $P_s/P_c$ changes by less than 1.5%, from 1.93 to 1.90. For $\eta \le 0.6$ the stick threshold in hysteresis form falls below the physical limit ($\Delta \cos_s = 1.95$ at $\eta = 0.6$), so sticking by hysteresis at the baseline speed becomes admissible. Changing the stiffness has a similar effect. With $\kappa = 4$ and 8 the return boundary moves to about 141 and 121 nm and the stick boundary to about 73 and 62 nm, while $P_s/P_c$ changes by less than 1%. The projection and the stiffness thus shift the absolute thresholds by tens of percent but leave the force ratio, the three-regime structure and the ordering of the predictions unchanged. Because both enter the same energy balance, a smaller $\eta$

can partly be absorbed into a recalibrated $\kappa$, and separating them requires the maximum spread at two or more impact speeds.

# 6 Discussion

## 6.1 Geometry-dependent resistance and deformation

Under the fixed-edge assumption, the analytical solution identifies pinning work as the main route by which spacing acts. A higher encounter density increases the outward work $PA$ and leaves less energy for deformation at the first maximum. The resulting decrease in $A$ follows directly from equation (22), with no need to interpolate a parameter map. At baseline, the increase in maximum spread from 1.5939 to 2.1915 across the spacing interval is a substantial change in the maximum effective extent, even though the viscous correction is small, and it is consistent with a radial deformation controlled by resistance.

The nonlinear spring also links the model to the inertia–capillary scaling. When the quartic energy dominates and resistance work is small, equation (9) gives $A \sim (4H/\kappa)^{1/4}$. With $H = \mathrm{We}/4$, the deformation increment scales as $\mathrm{We}^{1/4}$, the same exponent found by Clanet et al. [2]. The correspondence is asymptotic rather than an equivalence of the two models: here the spread factor is $1 + A$, and its prefactor depends on the generalized coordinate and on the stiffness calibration inherited from [13].

## 6.2 Radial arrest and recoverable energy

Maximum spread alone does not fix the recovery. Resistance removes energy on both the spreading and the recoil legs, which gives the returned-state budget $H = K_{\mathrm{return}} + 2PA$, and equation (23) shows that stronger resistance lowers the recovery under the exact zero-viscosity assumptions. For arrested trajectories, part of the energy remains in the deformed shape. Keeping this stored energy in the budget prevents a static deformation from being counted as recovered kinetic energy.

The boundary $a_c \approx 129$ nm marks the loss of radial return with positive speed in the fixed-edge scenario. It follows from the energy condition and the amplitude equation, so it does not depend on plotting resolution. Recovery is especially sensitive near this boundary, because the square-root relation between speed and return energy amplifies small energy changes. The weak-viscosity expansion therefore needs a finite margin from arrest; its accuracy at the representative returning cases does not carry over to the transition itself.

Real rebound involves further routes for momentum transfer. Non-axisymmetric recoil [10] and pancake bouncing [11] show that detachment need not coincide with recovery of the initial radial extent, and the liquid penetration and gas-mediated recovery discussed for nanowalls [12] lie outside the present state variables. The radial-return boundary should therefore be used to classify solutions of this model; predicting normal restitution would require a vertical coordinate and a contact-state criterion.

## 6.3 Closure uncertainty and parameter identification

The comparison of edge-scaling exponents shows that spacing is not an independent force parameter until its relation to the edge scale is specified. The three families coincide at the reference geometry yet extrapolate differently: fixed scaling gives $P \propto a^{-1}$, intermediate scaling weakens the trend, and proportional scaling removes it. These differences are structural. Numerical refinement can confirm that each family is evaluated accurately, but it cannot tell which family describes fabricated

nanowalls. The arrest window makes the point concrete: its spacing ratio is 1.93 for $\nu = 0$ but 3.72 for $\nu = 0.5$.

The force-scale scenarios make the same point. A factor-of-two change moves the fixed-edge boundary from about 129 nm to about 64 or 258 nm; these are deterministic alternatives, not statistical confidence limits. A measurement of maximum spread provides only one relation among stiffness, resistance and damping, and the amplitude equation cannot separate the product $D_e|\cos\theta^*|$. Independent characterization of the wall edges, advancing and receding angle measurements, and resolved spreading–recoil trajectories would each add constraints. Equations (24) and (25) show how a second observable from the same impact closes the problem, and the sensitivity analysis indicates where such a measurement is most informative. Two predictions do not depend on the closure at all: the peak residual extent $1 + A_s$ and the force ratio $P_s/P_c$. Neither involves $D_e|\cos\theta^*|$ or $\nu$. The spacing ratio $a_c/a_s$ is free of the force scale only at fixed $\nu$, and it is more useful for determining $\nu$ through equation (19) than for testing the model. A family of textures whose residual radial extent peaked at a height inconsistent with $1 + A_s$, or whose critical forces, identified independently through the inverse relations, had a ratio outside the bounds of equation (18), would falsify the saturated-pinning radial model itself, not merely one parameter value. The hysteresis form adds a further check. Below $a_{\mathrm{adm}} \approx 95$ nm the fixed-edge force exceeds what hysteresis can supply, and at the measured spacing of the surfaces of [12] the closure force is two orders of magnitude above the measured hysteresis force (Section 5.8).

The weak response to the width-to-pitch ratio is conditional in the same way, because the closure lets the solid fraction act only through damping. The damping multiplier varies from 1.0025 to 1.36 over the stated range and changes the spread by about 0.12% at 400 nm. This reflects the chosen solid-fraction closure and the small damping scale, and it does not rule out strong effects of wall height, connected-wall topology, compliance or a change of wetting state. The studies of Bartolo et al. [7] and Tsai et al. [8] show why geometric and wetting information must accompany any comparison between textured surfaces.

### 6.4 Quantitative predictions for experimental tests

Table 4 separates predictions that test the structure of the model from those that test its force closure. Predictions that depend only on $\kappa$ and $\eta$ test the energy structure of the model, and a disagreement with them would point to missing physics, such as finite smoothing, penetration or non-radial modes, rather than to a poorly chosen force parameter. The spacing ratio tests the force-scaling law through $\nu$, and the absolute spacings test the full closure. An experimental programme would thus proceed in a definite order: measure the wetting and test the force-threshold structure first, then determine $\nu$, and only then calibrate $C$.

### 6.5 Implications for applications

The regime structure suggests design hypotheses for the applications that motivated this study, which experiments would have to confirm. For surfaces meant to shed impacting drops, such as anti-icing and self-cleaning coatings, where impacting drops can also carry away surface dust [9], the model suggests keeping the pinning force below $P_c$, or equivalently the hysteresis below $\Delta\cos_c$. Within the model radial return is a necessary condition for shedding but not a sufficient one, because detachment, lift-off and post-impact adhesion are not resolved. For spray coating and deposition, where the aim is to keep liquid on the surface, the stick boundary is where the residual radial extent is largest; whether this also maximizes the wetted area or the retained volume depends on contact-line behaviour that the radial coordinate does not describe. The spacing that minimizes maximum

Table 4: Predictions of the saturated-pinning radial model at baseline (We = 18.3, $\kappa = 6$, $\eta = 1$), the observable that tests each, and the uncertain inputs on which each depends: the edge-force scale $C$, the edge-scaling exponent $\nu$, the stiffness $\kappa$ and the radial energy fraction $\eta$.

| Prediction | Baseline value | Observable | Depends on |
|---|---|---|---|
| Peak residual extent | $1 + A_s = 1.83$ | Residual projected extent of arrested drops (proxy), spacing series | $\kappa$, $\eta$ |
| Force-threshold ratio | $P_s/P_c = 1.93$, bounds 1.63–2.01 | Critical forces from the inverse relations at the two boundaries | $\kappa H$ only |
| Arrest-window spacing ratio | $a_c/a_s = 1.93$ ($\nu = 0$), 3.72 ($\nu = 0.5$) | Spacings where sticking and return first occur | $\nu$, weakly $\kappa H$ |
| Return threshold in hysteresis | $\Delta \cos_c = 1.47$ | Advancing and receding angles plus recoil | $\kappa$, $\eta$ |
| Maximum We for hysteretic sticking | about 11 | Impact-speed series on a high-hysteresis surface | $\kappa$, $\eta$ |
| Regime of the surfaces of [12] | Radial return, $e_r \approx 0.99$ | Retraction on those surfaces | Measured angles |
| Recoil time at return boundary | $1.23\tau \approx 10$ ms | Radius history near the transition | $\kappa$, $\eta$ |
| Stick and return spacings | about 67 and 129 nm ($\nu = 0$) | Spacing series | $C$, $\nu$, $\kappa$, $\eta$ |
| Admissibility spacing | about 95 nm ($\nu = 0$) | Independent edge-force estimate | $C$, $\nu$ |

spread is not the one that maximizes the residual radial extent, so the two objectives, if confirmed, would call for different textures. For thermal applications, where heat transfer depends on how the working fluid interacts with the heated surface, as in solar-pond heat-extraction coils [21], the energy partition indicates how much of the impact energy remains stored in the deformed drop at the end of the first cycle. Under the closure these statements become spacing criteria only for an assumed $\nu$ and $C$; in force or hysteresis form they are independent of the closure. The underlying relations are exact for the zero-viscosity model with saturated resistance and are verified numerically, which establishes their mathematical consistency, not their physical accuracy. The first-order extension gives the leading damping effect and retains both the viscous loss and the resulting shortening of the pinning path; their competition is the reason a damping correction cannot be obtained simply by subtracting viscous work along an unchanged trajectory.

For surface design, the analysis offers testable, conditional relations rather than a universal optimum spacing. The maximum spread is relevant to the area an impacting drop first covers, but rebound, rolling and contaminant removal depend on later translation, rotation and adhesion, and a favorable radial response need not maximize any of them. Experiments that distinguish spreading, recoil arrest, normal detachment and lateral motion can test each mechanism without mixing their observables, and the present framework gives a transparent basis for such comparisons and for extending the constitutive description.

### 6.6 Limitations and future work

The results carry the limitations of the model from which they are derived, and these define the most useful next steps.

*Single radial coordinate.* The model follows only the radial extent. It cannot represent vertical motion, lift-off, splashing or non-axisymmetric recoil, so $e_r$ is a radial recovery measure and not a coefficient of restitution. Adding a vertical degree of freedom with a contact-state criterion would allow rebound and contact time to be predicted and compared with the classical contact-time scaling [20].

*Saturated pinning and weak viscosity.* The exact results assume an ideal friction law ($\epsilon \to 0$) and zero viscosity, and the first-order correction is reliable only away from the return boundary. Viscous liquids, higher Weber numbers and finite smoothing of the pinning law would require a full treatment, for which the present solution provides a reference limit.

*Static and kinetic resistance.* The model uses one force both to resist motion and to hold the drop at rest. The comparison with [12] indicates that the two differ by about two orders of magnitude on real nanowalls. Separate static and kinetic capacities, with the motion followed beyond the first cycle, are the most direct extension.

*Fixed wetting state.* The Cassie state is prescribed. Impalement, gas drainage and wall compliance are not modeled, although the admissibility bound suggests that the fine-spacing regime may depend on them. A pressure-balance impalement criterion [7] could be coupled to the solution to make the wetting state an outcome of the impact rather than an input.

*Closure parameters.* The edge-force scale and its exponent have not been measured, the stiffness was calibrated at a single impact speed, and the solid-fraction relation $\phi = \alpha^2$ idealizes the wall network. The inherited force is about a hundred times the measured hysteresis force of the reference surfaces. The sensitivity analysis identifies which of these matters most at each spacing.

*Experimental validation.* The model has been checked against smooth-surface correlations and against the measured wetting of [12], but not against impact time histories on a spacing series of nanowalls. The minimum data set that would discriminate among the edge-scaling scenarios is the following: (i) advancing and receding angles on each texture, which fix the static capacity; (ii) $\beta_{\max}$ together with either the retraction speed or the arrested extent at one impact speed on at least three spacings, which through the inverse relations gives $P$ at each spacing and hence the slope $d\ln P/d\ln a = \nu - 1$, the third spacing testing the power law; and (iii) $\beta_{\max}$ on one texture at a second impact speed, which separates $\kappa$ from the energy fraction $\eta$. If both regime boundaries are observed, equation (19) gives $\nu$ directly. The absolute spacing boundaries and the admissibility spacing require $C$ and $\nu$ to be calibrated in this way, whereas the force thresholds, the hysteresis thresholds and the peak residual extent require only $\kappa$ and $\eta$. Imaging the contact line from below would in addition show how the residual radial extent relates to the residual wetted area. Extensions to later impact cycles, oblique impact, pillar and hierarchical textures, and icing conditions would follow naturally.

# 7 Conclusion

Whether an impacting drop stays on a textured surface or recoils matters for anti-icing, self-cleaning, spray deposition and cooling. We solved analytically the first impact cycle of a nonlinear radial oscillator with saturated contact-line pinning and examined which of its predictions survive the uncertainty of the geometric force closure. The main findings are as follows.

1. Two explicit critical forces separate sticking, recoil arrest and radial return of the effective radial coordinate, and a cubic gives the residual radial extent of arrested drops. Their ratio $P_s/P_c$ depends on $\kappa H$ alone and lies between 1.63 and 2.01.

2. The corresponding spacing ratio is $(P_s/P_c)^{1/(1-\nu)}$: 1.93 for a spacing-independent edge force,

3.72 for $\nu = 0.5$, and undefined for $\nu = 1$. It is independent of the edge-force magnitude at fixed $\nu$ but not of the scaling law, and observing both boundaries would determine $\nu$.

3. In hysteresis form, pinning cannot hold a drop at maximum spread above We $\approx 11$. The measured hysteresis of the nanowall surfaces of [12] gives $P \approx 0.04$ and places those impacts in radial return, consistent with the observed rebound, whereas the inherited closure gives $P \approx 4.4$, beyond any hysteresis. The closure therefore represents lumped dynamic resistance, and the spacing boundaries it produces (about 67 and 129 nm at We = 18.3 for $\nu = 0$) are scenario predictions.

4. Closed-form inverse relations recover the stiffness and pinning force from two observables of one impact. The pinning force is robust to measurement noise (about ±10–20% at 3% noise); the stiffness is not (−34% to +56%), and regime assignments close to the boundaries are uncertain.

5. The force ratio, the three-regime structure and the ordering of the predictions are insensitive to the energy projection and to stiffness values between 4 and 8, which move the absolute thresholds by tens of percent.

6. The residual radial extent peaks at the stick boundary, and pinning dissipates all of the impact energy at the return boundary, where the radial recoil time is largest ($1.23\tau$).

These results are design hypotheses, not validated performance criteria. Radial return is not detachment or rebound, and a large residual radial extent does not by itself mean a large wetted area or retained volume. The analysis applies to a single radial coordinate with saturated pinning, weak viscosity and a prescribed Cassie state. Measuring advancing and receding angles, maximum spread and retraction on a spacing series of nanowalls at two impact speeds, and extending the model with separate static and kinetic resistances and a vertical degree of freedom, are the most important next steps.

## Data and code availability

All results are computed from the equations given in this paper. The Python scripts that evaluate the analytical solution, perform the independent ODE integrations, the Sobol analysis and the noise, energy-projection and stiffness analyses, and generate every figure, together with their numerical outputs, are provided as Supplementary Material and are available from the corresponding author on request.

## References


[1] Josserand, C.; Thoroddsen, S.T. Drop impact on a solid surface. *Annual Review of Fluid Mechanics* **2016**, 48, 365–391. https://doi.org/10.1146/annurev-fluid-122414-034401

[2] Clanet, C.; Béguin, C.; Richard, D.; Quéré, D. Maximal deformation of an impacting drop. *Journal of Fluid Mechanics* **2004**, 517, 199–208. https://doi.org/10.1017/S0022112004000904

[3] Okumura, K.; Chevy, F.; Richard, D.; Quéré, D.; Clanet, C. Water spring: A model for bouncing drops. *Europhysics Letters* **2003**, 62, 237–243. https://doi.org/10.1209/epl/i2003-00340-1

[4] Kim, H.-Y.; Chun, J.-H. The recoiling of liquid droplets upon collision with solid surfaces. *Physics of Fluids* **2001**, 13, 643–659. https://doi.org/10.1063/1.1344183

[5] Cassie, A.B.D.; Baxter, S. Wettability of porous surfaces. *Transactions of the Faraday Society* **1944**, 40, 546–551. https://doi.org/10.1039/TF9444000546

[6] Wenzel, R.N. Resistance of solid surfaces to wetting by water. *Industrial & Engineering Chemistry* **1936**, 28, 988–994. https://doi.org/10.1021/ie50320a024

[7] Bartolo, D.; Bouamrirene, F.; Verneuil, E.; Buguin, A.; Silberzan, P.; Moulinet, S. Bouncing or sticky droplets: Impalement transitions on superhydrophobic micropatterned surfaces. *Europhysics Letters* **2006**, 74, 299–305. https://doi.org/10.1209/epl/i2005-10522-3

[8] Tsai, P.; Pacheco, S.; Pirat, C.; Lefferts, L.; Lohse, D. Drop impact upon micro- and nanostructured superhydrophobic surfaces. *Langmuir* **2009**, 25, 12293–12298. https://doi.org/10.1021/la900330q

[9] Abubakar, A.A.; Yilbas, B.S.; Yakubu, M.; Al-Qahtani, H.; Hassan, G.; Adukwu, J.E. Impacting droplet can mitigate dust from PDMS micro-post array surfaces. *Coatings* **2021**, 11, 1377. https://doi.org/10.3390/coatings11111377

[10] Bird, J.C.; Dhiman, R.; Kwon, H.-M.; Varanasi, K.K. Reducing the contact time of a bouncing drop. *Nature* **2013**, 503, 385–388. https://doi.org/10.1038/nature12740

[11] Liu, Y.; Moevius, L.; Xu, X.; Qian, T.; Yeomans, J.M.; Wang, Z. Pancake bouncing on superhydrophobic surfaces. *Nature Physics* **2014**, 10, 515–519. https://doi.org/10.1038/nphys2980

[12] Yilbas, B.S.; Abubakar, A.; Yakubu, M.; Al-Qahtani, H.; Al-Sharafi, A. Nanowall textured hydrophobic surfaces and liquid droplet impact. *Materials* **2022**, 15, 1645. https://doi.org/10.3390/ma15051645

[13] Ismail, N.A.; Yakubu, M. Droplet Spreading on Nanowall-Textured Hydrophobic Surfaces: A Nonlinear Reduced-Order Model. *Research Square*, preprint, version 1, **2026**. https://doi.org/10.21203/rs.3.rs-11221595/v1

[14] Den Hartog, J.P. Forced vibrations with combined Coulomb and viscous friction. *Transactions of the American Society of Mechanical Engineers* **1931**, 53, 107–115.

[15] Furmidge, C.G.L. Studies at phase interfaces. I. The sliding of liquid drops on solid surfaces and a theory for spray retention. *Journal of Colloid Science* **1962**, 17, 309–324. https://doi.org/10.1016/0095-8522(62)90011-9

[16] Saltelli, A.; Annoni, P.; Azzini, I.; Campolongo, F.; Ratto, M.; Tarantola, S. Variance based sensitivity analysis of model output. Design and estimator for the total sensitivity index. *Computer Physics Communications* **2010**, 181, 259–270. https://doi.org/10.1016/j.cpc.2009.09.018

[17] Laan, N.; de Bruin, K.G.; Bartolo, D.; Josserand, C.; Bonn, D. Maximum diameter of impacting liquid droplets. *Physical Review Applied* **2014**, 2, 044018. https://doi.org/10.1103/PhysRevApplied.2.044018

[18] Antonini, C.; Amirfazli, A.; Marengo, M. Drop impact and wettability: From hydrophilic to superhydrophobic surfaces. *Physics of Fluids* **2012**, 24, 102104. https://doi.org/10.1063/1.4757122

[19] Bartolo, D.; Josserand, C.; Bonn, D. Retraction dynamics of aqueous drops upon impact on non-wetting surfaces. *Journal of Fluid Mechanics* **2005**, 545, 329–338. https://doi.org/10.1017/S0022112005007184

[20] Richard, D.; Clanet, C.; Quéré, D. Contact time of a bouncing drop. *Nature* **2002**, 417, 811. https://doi.org/10.1038/417811a

[21] Yakubu, M.; Shuja, S.Z.; Yilbas, B.S.; Al-Qahtani, M. Influence of working fluid on a novel solar pond coil. *Journal of Energy Resources Technology* **2021**, 143, 042105. https://doi.org/10.1115/1.4048260